Correlation Tensor MRI deciphers underlying kurtosis sources in stroke

Rita Alves [a], Rafael Neto Henriques [a], Leevi Kerkelä [b], Cristina Chavarrías [a], Sune N Jespersen [c,d], Noam Shemesh [a,*]

[a] *Champalimaud Research, Champalimaud Centre for the Unknown, Lisbon, Portugal*
[b] *UCL Great Ormond Street Institute of Child Health, University College London, London, United Kingdom*
[c] *Center of Functionally Integrative Neuroscience (CFIN) and MINDLab, Clinical Institute, Aarhus University, Aarhus, Denmark*
[d] *Department of Physics and Astronomy, Aarhus University, Aarhus, Denmark*

ABSTRACT

Noninvasively detecting and characterizing modulations in cellular scale micro-architecture remains a *desideratum* for contemporary neuroimaging. Diffusion MRI (dMRI) has become the mainstay methodology for probing microstructure, and, in ischemia, its contrasts have revolutionized stroke management. Diffusion kurtosis imaging (DKI) has been shown to significantly enhance the sensitivity of stroke detection compared to its diffusion tensor imaging (DTI) counterparts. However, the interpretation of DKI remains ambiguous as its contrast may arise from competing kurtosis sources related to the anisotropy of tissue components, diffusivity variance across components, and microscopic kurtosis (e.g., arising from cross-sectional variance, structural disorder, and restriction). Resolving these sources may be fundamental for developing more specific imaging techniques for stroke management, prognosis, and understanding its pathophysiology. In this study, we apply Correlation Tensor MRI (CTI) – a double diffusion encoding (DDE) methodology recently introduced for deciphering kurtosis sources based on the unique information captured in DDE's diffusion correlation tensors – to investigate the underpinnings of kurtosis measurements in acute ischemic lesions. Simulations for the different kurtosis sources revealed specific signatures for cross-sectional variance (representing neurite beading), edema, and cell swelling. *Ex vivo* CTI experiments at 16.4 T were then performed in an experimental photothrombotic stroke model 3 h post-stroke ($N = 10$), and successfully separated anisotropic, isotropic, and microscopic non-Gaussian diffusion sources in the ischemic lesions. Each of these kurtosis sources provided unique contrasts in the stroked area. Particularly, microscopic kurtosis was shown to be a primary "driver" of total kurtosis upon ischemia; its large increases, coupled with decreases in anisotropic kurtosis, are consistent with the expected elevation in cross-sectional variance, likely linked to beading effects in small objects such as neurites. *In vivo* experiments at 9.4 T at the same time point (3 h post ischemia, $N = 5$) demonstrated the stability and relevance of the findings and showed that fixation is not a dominant confounder in our findings. In future studies, the different CTI contrasts may be useful to address current limitations of stroke imaging, e.g., penumbra characterization, distinguishing lesion progression form tissue recovery, and elucidating pathophysiological correlates.

1. Introduction

Progressive modulations in neural tissue micro-architecture are associated with diverse processes including development (Suter and Jaworski, 2019), plasticity (Hughes et al., 2018), memory (Brodt et al., 2018), learning (Scholz et al., 2009; Zatorre et al., 2012), connectivity between brain areas (Craddock et al., 2013; Pestilli et al., 2014), aging (Hill et al., 2018), and recovery from injury (Murphy and Corbett, 2009). Adverse micro-architectural alterations in the neural tissue milieu are also linked to psychiatric disorders such as depression (Li et al., 2010),

neurodegenerative diseases such as Parkinson's disease (Peelaerts et al., 2015) and Alzheimer's disease (De Strooper and Karran, 2016), and injuries such as ischemic stroke (Murphy and Corbett, 2009) and traumatic brain injury (Budde et al., 2011). Ischemic stroke – one of the leading causes of disability and death worldwide (Mathers et al., 2017) – involves a complex cascade of events occurring acutely following a blood vessel occlusion and the ensuing metabolic and aerobic deprivation (Belov Kirdajova et al., 2020). The ischemic cascade leads to micro-architectural modifications including neurite beading (Takeuchi et al., 2005; Enright et al., 2007; Budde and Frank, 2010; Skinner et al., 2015; Kislin et al., 2017), cytotoxic edema (Simard et al., 2007) – causing intracellular swelling due to loss of ion homeostasis – and cell death (Ferrer and Planas, 2003) (Fig. 1A), followed later by blood-brain barrier disruptions (Piao et al., 2009; Yang and Rosenberg, 2011) and va-
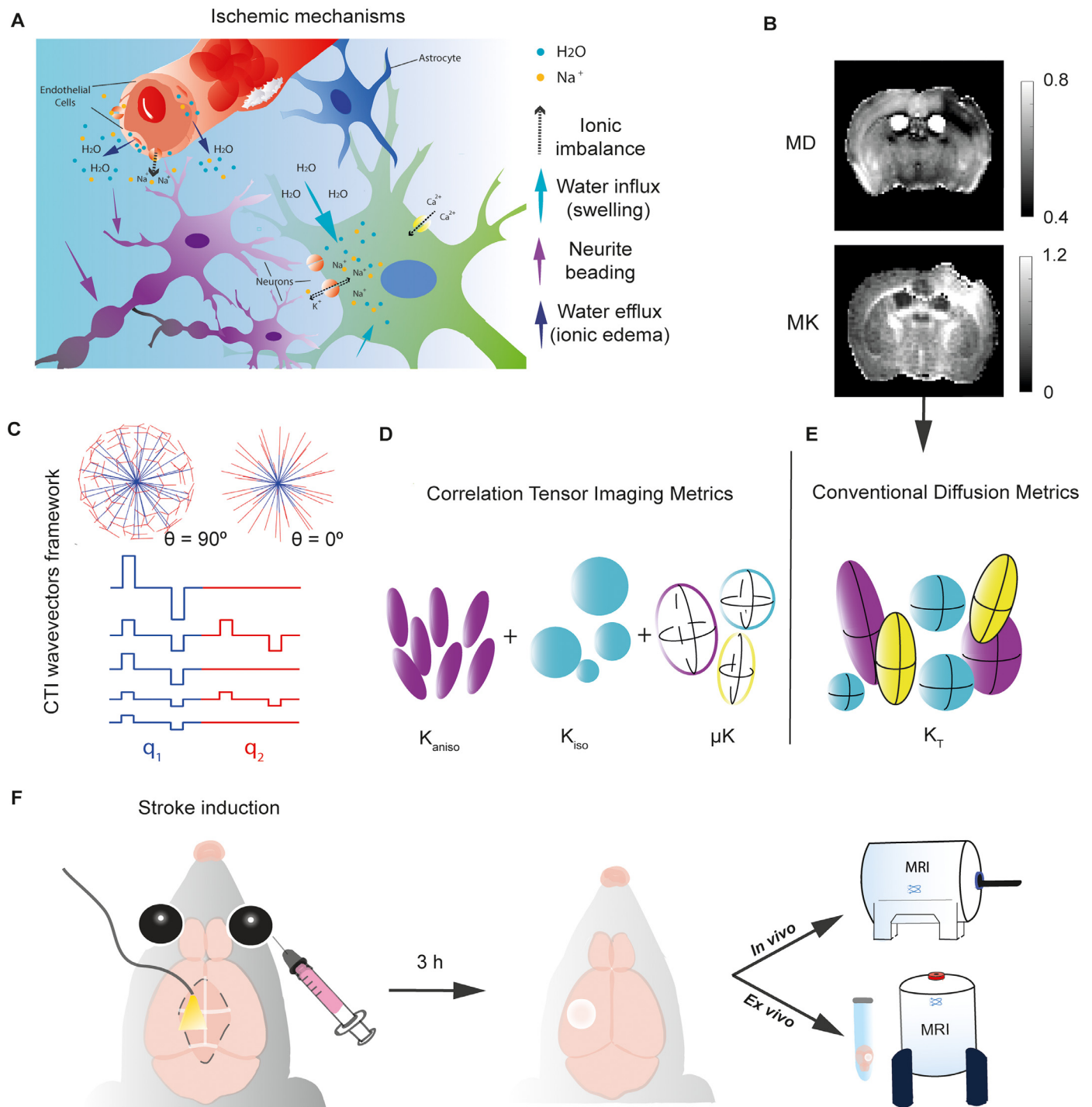
Fig. 1. Acute ischemic mechanisms, CTI, and stroke experimental set up. (A) In the acute ischemic phase, microscopic disturbances such as ionic imbalance (dashed arrows) and excessive cellular water influx result in cell swelling (light blue arrows) and neurite beading (purple), collectively referred to as cytotoxic edema. This is followed by ionic edema – transcapillary flux of Na^+ and water efflux (dark blue arrows). The blood brain barrier remains intact at this acute stage. (B) MD [0.4 0.8] (μm^2/ms and total kurtosis (K_T) [0 1.2] from conventional SDE delineate the lesion but cannot resolve the different kurtosis sources. (C) Correlation Tensor MRI (CTI), with different combinations of wavevectors (q_1 and q_2) disentangles the underlying kurtosis sources, namely, the contributions from (D): Anisotropic Kurtosis, K_{aniso}; Isotropic Kurtosis, K_{iso}; and Microscopic Kurtosis, μK. (F) A photothrombotic model was used to induce a well delimited and reproducible focal infarct. Upon longitudinal incision and target region coordinates identification (S1bf), irradiation on the left hemisphere was performed for 15 min. At 3 h post irradiation offset, the brains were either imaged *in vivo* or fixed via transcardial perfusion, extracted and placed in an NMR tube with Fluorinert for MRI imaging.

sogenic edema (Simard et al., 2007). The extent of these processes can later contribute to the prognosis and potential for functional recovery (Zeiler et al., 2016) and/or efficacy of treatment.

Since the 1990′s, diffusion MRI (dMRI) has played a pivotal role in mapping ischemia noninvasively. The Apparent Diffusion Coefficient (ADC) was shown to decrease as early as a few minutes after stroke onset (Moseley et al., 1990a, 1990b; Warach et al., 1992, 1995), thereby revolutionizing the diagnosis, prognosis, and management of stroke (Moseley et al., 1990a, 1990b; Karbasforoushan et al., 2019) and facilitating the administration of treatment within the limited time window of operation.

Despite the sensitivity of ADC to early ischemia, the pathophysiology underlying these ADC changes remains vigorously debated (Moseley et al., 1990a, 1990b; Duong et al., 1998; Silva et al., 2002; Le Bihan, 2007; Goodman et al., 2008; Budde and Frank, 2010; Jelescu et al., 2014; Novikov et al., 2014). In particular, the ADC (as well as its rotationally invariant counterparts) lacks specificity to the underlying tissue microstructural changes, which potentially involve a combination of neurite beading, cell swelling, extra/intra-cellular space imbalances, intrinsic diffusivity variations, mitochondrial beading, neurite orientation dispersion, myelination, and other effects. This lack of specificity limits the interpretation of the findings (Fig. 1B). Arguably one of the most important limitations of conventional dMRI methods pertains to the identification of the core and penumbra of the ischemic insult (Campbell et al., 2012). Moreover, such metrics are limited for assessing the evolution of ischemic lesions and for predicting functional outcomes. Indeed, longitudinal stroke studies showed that ADC pseudo-normalizes by the evolution of cell death and the appearance of vasogenic edema (Warach et al., 1995), and thus it cannot unambiguously distinguish between subacute and chronic stroke phases. Attempts to enhance the information derived from dMRI included applying more advanced signal representations and models to data acquired for multiple diffusion gradient directions and b-value weightings (e.g. Basser et al., 1994; Jensen et al., 2005; Fieremans et al., 2011; Zhang et al., 2012). Measurements of fractional anisotropy (FA) from diffusion tensor imaging (DTI) (Basser et al., 1994) showed that the diffusion anisotropy in white matter regions with high directional coherence decreases post-stroke, possibly reflecting irreversible degeneration processes (van der Zijden et al., 2008), while increases in diffusion anisotropy in perilesional and contralateral regions were potentially representative of white matter remodeling (Moura et al., 2019). FA, however, is only useful in well aligned white matter regions and further studies have shown that DTI provides low added value in stroke management comparatively to simpler ADC estimates (Moura et al., 2019).

Another advance in dMRI imaging of stroke involved the application of diffusion kurtosis imaging (DKI) (Jensen et al., 2005), and neurite density and dispersion orientation imaging (NODDI; Zhang et al., 2012), which showed that quantities based on the degree of non-Gaussian diffusion signals can be more sensitive to ischemic lesions than ADC (Adluru et al., 2014; Grinberg et al., 2012; Hui et al., 2012b) and less affected by vasogenic diffusion effects in subacute phases (Hui et al., 2012a; Moura et al., 2019). However, although the sensitivity was enhanced, the specificity remained low in these single diffusion encoding (SDE) (Stejskal and Tanner, 1965; Shemesh et al., 2016) based techniques, and their interpretation remains highly ambiguous (Umesh Rudrapatna et al., 2014).

The main caveat of DKI is that different kurtosis sources are all conflated in the DKI metrics (Jensen et al., 2005; Lasič et al., 2014; Paulsen et al., 2015; Szczepankiewicz et al., 2016; Henriques et al., 2020). Sources of non-mono-Gaussian (with wavevector q, or non-mono-exponential with diffusion weighting b) diffusion signals include:

- Variance in diffusion tensor eigenvalues, leading to effects typically termed "anisotropic kurtosis" (K_{aniso}); In particular, K_{aniso} quantifies the degree of microscopic anisotropy in the tissue irrespec-

tive of orientation dispersion effects and/or microscopic kurtosis (Henriques et al., 2021b)

- Variance in the magnitude of diffusion tensors e.g., arising from a distribution of diffusion tensor traces, leading to effects typically termed "isotropic kurtosis" (K_{iso}) (Eriksson et al., 2013; Szczepankiewicz et al., 2015; Nilsson et al., 2020); K_{iso} quantifies the variance in the sizes of the diffusion microenvironments;

- Microscopic kurtosis (μK), arising from cross-sectional variance and/or structural disorder (Novikov and Kiselev, 2010; Lee et al., 2020), leading to positive effects ($\mu K>0$) (Novikov and Kiselev, 2010; Burcaw et al., 2015) or arising from fully restricted diffusion (Callaghan et al., 1991; Assaf and Cohen, 1998; Torres et al., 1999), which can lead under some conditions to negative effects, ($\mu K<0$).

We note that exchange effects can also appear as μK in some cases, and that all kurtosis sources can be modulated by exchange. Since all the underlying kurtosis sources are conflated in SDE, and any combination can potentially lead to identical total kurtosis values, the SDE signal does not carry sufficient information for resolving the contribution of the underlying kurtosis sources. This can have significant impact on understanding the origins of progressive microstructural modulations. In stroke, for example, effects arising from cross-sectional variations, e.g., due to neurite beading (Takeuchi et al., 2005; Budde and Frank, 2010; Buscemi et al., 2019; Lee et al., 2020); (Fig. 1A, purple), changes in diffusivity distributions due to e.g., cell body swelling (Xing et al., 2012) (Fig. 1A, light blue) or the transcapillary ionic edema (Stokum et al., 2016) (Fig. 1A, dark blue), are notoriously difficult to decipher (Fig. 1B, E). Resolving these scenarios could be fundamental for stroke management and prognosis.

Here, we depart from the convention of mapping the diffusion properties using SDE, and rather endeavor to explicitly resolve the kurtosis sources from Correlation Tensor MRI (Henriques et al., 2020; Fig. 1C), a recently introduced methodology harnessing the cumulant expansion of Double Diffusion Encoding (DDE) signals (Jespersen and Buhl, 2011; Jespersen, 2012; Jespersen et al., 2013) to directly disentangle the kurtosis sources (Fig. 1D). DDE applies two independent diffusion-sensitizing gradient pulse pairs that span two diffusion epochs, separated by a mixing time, in which the correlation between diffusion-driven displacements can be probed in multiple directions (Mitra, 1995; Cheng and Cory, 1999; Koch and Finsterbusch, 2008; Finsterbusch, 2011; Shemesh et al., 2012; Jespersen et al., 2013; Shemesh et al., al.,2014; Shemesh et al., 2016). The cumulant expansion of the DDE signals involves higher order tensors (Jespersen and Buhl, 2011; Jespersen, 2012; Jespersen et al., 2013), which in the long mixing time, include the rank 4 Z tensor, directly delivering information on K_{aniso} and K_{iso}, as well as the conventional rank 4 kurtosis tensor, W, which provides information on the total kurtosis, containing the conflated K_{aniso}, K_{iso}, and μK. By directly estimating W and Z, CTI is thus able to explicitly disentangle the different underlying sources contributing to total kurtosis. We hypothesize that these different sources can distinguish different scenarios underpinning SDE contrasts in stroke, and thus that CTI may mitigate the current specificity limitations and assist in characterizing the lesion, which in the future could assist in understanding the extent of salvageable penumbra, distinguish lesion progression and provide means to quantify tissue recovery. The first CTI experiments in subacute ischemic lesions are presented in a photothrombotic rodent model of stroke, evidencing unique signatures for the different underlying micro-architectural modulations, which are shown to be consistent with cross-sectional variance of small structures, likely reflecting neurite beading distinguishable from large cellular-scale swelling, and edema. CTI thus delivers the sought-after specificity towards important microstructural features, which can impact our understanding the progressive modulations occurring in tissue in health and disease.

2. Materials and methods

2.1. Simulations

Given the potential complexity of diffusion modes in tissue, we note for clarity that "components" involve microenvironments with Gaussian diffusion, and "compartments" are associated with restricted diffusion (irrespective of an association with e.g., specific biological compartments such as intra/extra axonal water, etc.).

Monte Carlo simulations were performed to investigate specific signatures for: 1) neurite beading; 2) edema; 3) cell swelling. These microstructural scenarios were simulated in two steps: first, the diffusivities and kurtosis of each component were simulated for individual microstructural environments (e.g. representing diffusion in biological compartments such as intra-axonal spaces extra-axonal spaces or within spherical cells, etc.), and then, to mitigate the dependence of these simulations on the specifics of CTI experimental parameters, the kurtosis sources were computed in a forward model fashion using their ground truth definitions as given in Henriques et al. (2020). Briefly, those are defined as: $K_{aniso} = 2\langle \frac{\mu A_i^2}{D_i^2} \rangle$ where $\langle \rangle$ represents the ensemble average, μA_i is the microscopic anisotropy of microenvironment i, D_i is the mean diffusivity associated to microenvironment i; $K_{iso} = 3\frac{V(D_i)}{D^2}$, where $V(D_i)$ represents the variance across the mean diffusivities of microenvironment D_i, and D is the total mean diffusivity; and $\mu K = \frac{\langle D_i^2 \mu K_i \rangle}{D^2}$; where μK_i is the microscopic kurtosis of individual compartment i. In all cases, exchange was assumed to be negligible.

Neurite beading: A neurite without beading was first modelled as an impermeable cylinder (length = 31.4 μm, radius = 1 μm) aligned with the z-axis. Beading was introduced by making the radius depend on the location along the z-axis: r(z) = r$_0$ + Asin(Bz), where r$_0$ is the mean radius, A $\in$ [0,1] controls the amplitude of beading, and B controls the frequency of beading. Five simulated neurites, shown in Fig. 2A, were generated by increasing A from 0 to 0.8 in equal steps and adjusting r$_0$ to keep the volume constant. B = 1 μm^{-1} for all simulated neurites.

Synthetic data was generated using Disimpy (Kerkelä et al., 2020) with 10^5 random walkers, 10^4 time steps, and diffusivity of 2 μm^2/ms. The initial positions of the random walkers were randomly sampled from a uniform distribution inside the axons. MR signals were generated using pulsed gradient single diffusion encoding with δ = 1.5 ms and Δ = 10 ms, 60 diffusion encoding directions uniformly distributed over the surface of half a sphere, and 10 b-values uniformly distributed between 0 and 3 ms/μm^2. The individual mean diffusivity and kurtosis are extracted from the DKI tensors fitted to these signals using a weighted linear least squares fit in Dipy (Garyfallidis et al., 2014; Henriques et al., 2021a).

Edema: Formation of edema was simulated by adding a free water component (individual diffusivity = 3 μm^2/ms and kurtosis = 0) with varying volume fraction with the most beaded scenario previously simulated with A = 0.8 (Fig. 2B).

Cell swelling: Individual diffusivities and kurtosis of spherical compartments with restricted diffusion are first computed from synthetic signals using MISST toolbox (Drobnjak et al., 2010, 2011; Ianuş et al., 2013, 2016). Spheres were simulated for a fixed size distribution (to model cell swelling) and formation of edema by adding a free water component with increasing volume fraction (Fig. 2C).

Extracellular space (ECS) simulations: The simulations in the Supplementary Information were performed by packing different beaded geometries, ensuring that they cannot intersect, and then simulations proceeded as mentioned above in the "neurite beading" subsection only for spins in the ECS.

2.2. Animals

All animal experiments were preapproved by the competent institutional and national authorities and carried out according to European Directive 2010/63. Adult male C57BL/6 J mice (N = 20 ~11 weeks old, weights 24–29 g, grown with a 12 h /12 h light/dark cycle with *ad libitum* access to food and water) were used in this study. N = 10 were used for the *ex vivo* study, N = 5 were used as controls (sham) for the *ex vivo* study, and N = 5 were used for the *in vivo* study.

2.3. Surgical procedures

A photothrombotic Rose Bengal stroke model (Watson et al., 1985) was used to induce a focal infarction in the barrel cortex (S1bf) in fifteen mice (N = 15), previously identified upon anatomic mapping, with a solution of Rose Bengal dye (Sigma Aldrich, 95%) dissolved in sterile saline (15 mg/ml) and filtrated through a 0.2 μm sterile filter. Each mouse was injected with meloxicam (Nonsteroidal anti-inflammatory drug) 30 min prior to surgery and anesthetized with isoflurane ($\sim$ 2.5% in 28% oxygen). Temperature was monitored and maintained at 36 – 37 °C with a heating pad. The skull was exposed by a median incision of the skin at the dorsal aspect of the head and the periosteum was removed (note that this procedure does not involve craniectomy).

The solution was delivered intravenously by a retroorbital injection (10 μl/g animal weight). The animals were then irradiated with a cold light source and a fiber optic light guide (0.89 mm tip) – reaching a color temperature of 3200 K and a beam light intensity of 10 W/cm^2 – in the barrel cortex (1.67 mm posterior; 3 mm lateral to bregma (Franklin and Paxinos, 2019)) for 15 min. A sham group (N = 5) underwent the same conditions except for the lesion-inducing illumination, yet the 15-minute interval post injection was respected.

2.4. Brain extraction and sample preparation

Brain specimens were fixed via transcardial perfusion with 4% Paraformaldehyde (PFA) and extracted from fifteen mice (N = 10 from the stroke group and N = 5 from the sham group) at 3 h post ischemic onset. After extraction from the skull, the brains were immersed in a 4% PFA solution for 24 h and washed in a Phosphate-Buffered Saline solution afterwards, preserved in for at least 24 h. The specimens were subsequently placed in a 10-mm NMR tube filled with Fluorinert (Sigma Aldrich, Lisbon, PT), secured with a stopper to prevent from floating. The tube was then sealed with paraffin film.

2.5. Ex vivo *MRI experiments*

Scans are first performed on the N = 15 fixed brain samples to characterize stroke lesions with higher data quality (higher resolution, SNR) and to avoid the effects of ongoing stroke lesion development and minimize physiological noise artefacts. All these *ex vivo* MRI scans were performed on a 16.4 T Aeon Ascend Bruker scanner (Karlsruhe, Germany) equipped with an AVANCE IIIHD console, a Micro5 probe with gradient coils capable of producing up to 3000 mT/m in all directions, and a birdcage RF volume coil. Once inserted, the samples were maintained at 37 °C using the probe's variable temperature capability, and the samples were allowed to acclimatize with the surroundings for at least 2 h prior to the beginning of diffusion MRI experiments. A B$_0$ map was also acquired covering the entire volume of the brain for shimming purposes.

DDE data were subsequently acquired for 25 coronal slices using an in house written EPI-based DDE pulse sequence implemented in Paravision 6.0.1 (Bruker BioSpin MRI GmbH, Ettlingen, Germany) and TopSpin 3.1. Details for the in house written DDE sequence and its validation (e.g. robustness to concomitant fields) was reported in (Ianus et al., 2018). Diffusion encoding gradient pulse separation Δ and mixing time τ_m were set to 10 ms, and the pulsed gradient duration δ was set to 1.5 ms. Acquisitions were repeated for five G$_1$-G$_2$ magnitude combinations (1498 - 0, 1059.2 - 1059.2, 1059.2 - 0, 749.0 - 749.0 and 749.0 - 0 mT/m) corresponding to b-values of 3000 - 0, 1500 - 1500, 1500 - 0, 750 - 750 and 750 - 0 s/mm^2. The maximum b-value = 3000 s/mm^2 was selected according to Henriques et al. (2021b) where this value
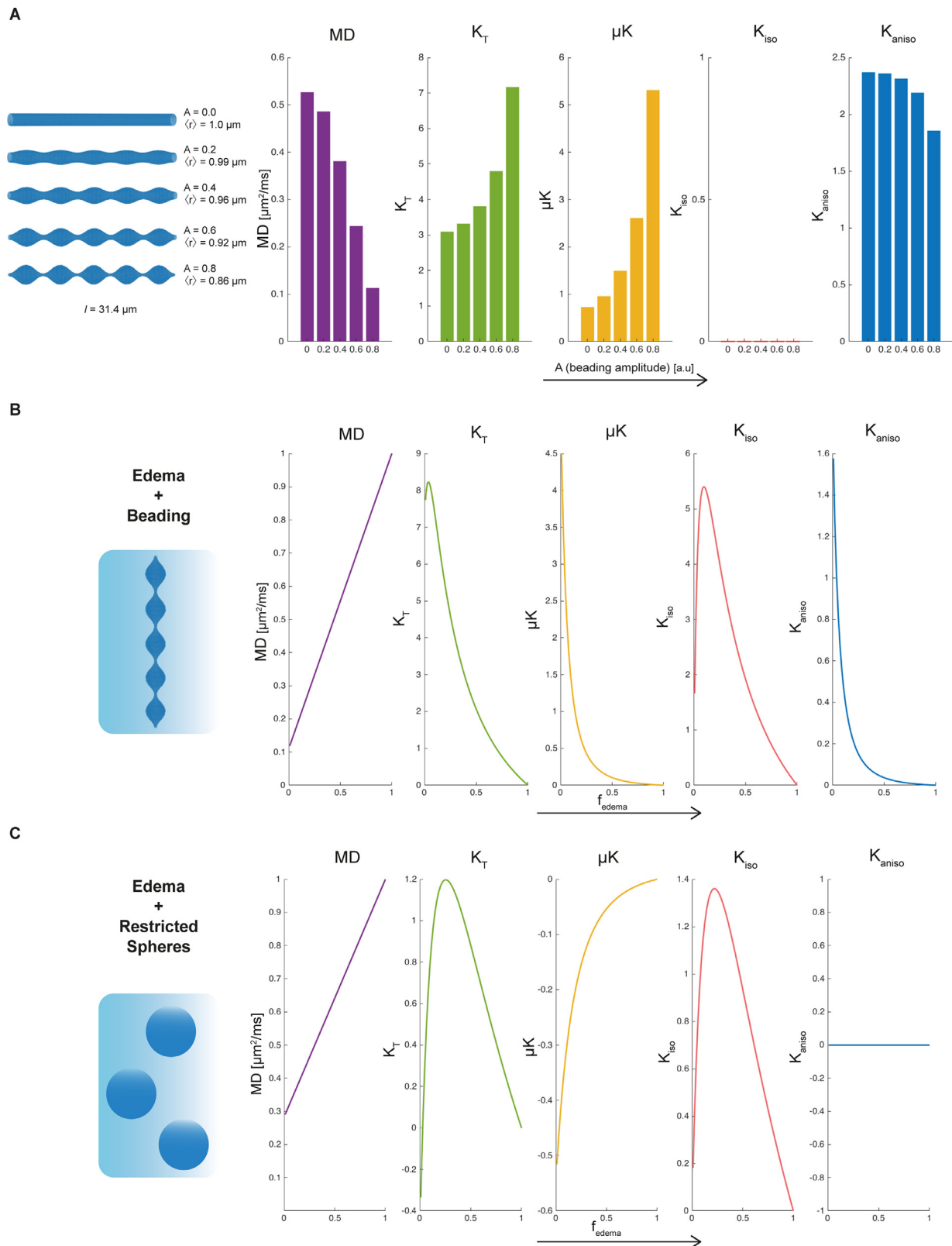
Fig. 2. Simulations for kurtosis sources in beading scenarios, restricted diffusion, and free water fraction addition. (A) Monte Carlo random walk simulations investigating the effect of "axon" beading on the diffusion kurtosis parameter estimates. Five simulated axons were generated by increasing A (which controls the amplitude of beading) from 0, i.e., axons without beading, to 0.8, axons with strong beading (the length was kept fixed at 31.4 μm). The respective conventional DKI and novel CTI diffusion kurtosis metrics are presented for all simulated axons scenarios (from left to right: MD [μm2/ms], K_T, μK, K_{iso}, K_{aniso}). Note that K_{iso} is zero by definition. (B) Kurtosis estimates simulated in a scenario of beading effects (A = 0.8) with increasing free water fraction (representing e.g. tissue beading and increasing edema). (C) Similar simulations of kurtosis estimates but now arising from diffusion in fully restricted spheres with a generalized Pareto Distribution approximation size distribution (μ= 0.75 ± 0.2 μm) over a range of 100 b-values as free water fraction increases (emulating cell swelling as edema increases).

was shown to provide an optimal trade-off between minimization of high order effects (accuracy) and maximization of the robustness of our measurements to noise (precision). Acquisition with $q_2=0$ were acquired for 135 directions for q_1, while equal magnitude q_1-q_2 combinations were repeated for 135 parallel and perpendicular directions as described by Henriques et al. (2021b). These DDE acquisition protocols are required for CTI reconstruction (Henriques et al., 2020,2021b). In addition, twenty acquisitions without any diffusion sensitization (zero b-value) were performed for each q_1-q_2 magnitude combination to guarantee a high ratio between the number of non-diffusion and diffusion-weighted acquisitions, such that the normalization with the non-diffusion weighted images is more robust. For all experiments, the following parameters were used: TR/TE = 3000/49 ms, Field of View (FOV) = 11×11 mm^2, matrix size 78×78, resulting in an in-plane voxel resolution of 141×141 μm^2, slice thickness = 0.5 mm, number of segments = 2, number of averages = 8. For every experiment, the acquisition time was approximately 1 h and 57 min (total of $\sim$ 14 h).

Axial and sagittal T2-weighted images with high resolution and high SNR were acquired for anatomical reference. These data were acquired using RARE pulse sequences with the following parameters: TR = 4000 ms, TE = 50 ms, RARE factor = 12, number of averages = 6. For the axial images, the FOV was 18×18 mm^2, and the matrix size was 240×132, resulting in an in-plane voxel resolution of 75×76 μm^2. For the sagittal images, FOV was set to 18×9 mm^2, matrix size to 240×120, and the in-plane voxel resolution was 75×75 μm^2 (sagittal). Both axial and sagittal acquisitions sampled the total of 33 slices with a thickness of 0.3 mm. For the coronal images, FOV was set to 10.5×10.5 mm^2, the matrix size was 140×140, resulting in an in-plane voxel resolution of 75×75 μm^2, for 72 slices 0.225 mm thick.

2.6. In vivo experiments

To confirm that our results were not confounded by fixation effects, MRI experiments were also performed *in vivo*. A cohort of $N = 5$ animals were scanned 3 h after ischemia induction using a 9.4 T Biospec Bruker scanner (Karlsruhe, Germany) equipped with an AVANCE IIIHD console and a Micro5 probe with gradient coils capable of producing up to 600 mT/m in all directions, an 86 mm quadrature coil for transmission and a 4-element array surface cryocoil for reception.

For anesthesia induction, the body temperature of the mouse was kept constant by placing the animal on top of an electrical heating pad. A mixture of medical air and 4% isoflurane (Vetflurane, Virbac, France) was maintained until the animal righting reflex and any reaction to firm foot squeeze were lost. The isoflurane concentration was regulated and reduced to 2.5%. The mouse was then weighed and transferred to the animal bed, prone positioned above a heated water pad (for the mouse body temperature not to oscillate during the experiments) with its head placed with its upper incisors held on to a mouth bite bar. Oxygen concentrations were kept between 50% and 52%, monitored by a portable oxygen monitor (MX300-I, Viamed, United Kingdom). Ear bars were used for a safe and efficient head fixation (into external meatus) and eye ointment (Bepanthen Eye Drops, Bepanthen, Germany) was applied to prevent the corneas from drying. A rectal temperature probe and a respiration sensor (Model 1030 Monitoring Gating System, SAII, United States of America) were placed for real-time monitoring of these physiological measurements to guarantee the animal's welfare and immobilization. The waterbed temperature was cautiously monitored and controlled to avoid oscillations. Respiration rates were also monitored and maintained at physiological levels throughout dMRI scanning.

Double diffusion encoding data was acquired using the same in house written EPI-based DDE pulse sequence with parameters optimized for *in vivo* experiments: 5 coronal slices; $\Delta = \tau_m = 10$ ms, $\delta = 4$ ms, six G_1-G_2 magnitude combinations (549.01 – 0, 388.21 – 388.21, 586.91 – 0, 415.01 – 415.01, 415.01 – 0, 388.21 – 0 mT/m), using the same directions as in the *ex vivo* experiments, 23 acquisitions without any diffusion-weighted sensitization (*b*-value = 0 mT/m) interspersed along

the entire experiment, TR/TE = 3000/58 ms, FOV = 17×12 mm^2, matrix size 92×66 (resulting in an in-plane voxel resolution of 181×181 μm^2), slice thickness = 0.85 mm, number of segments = 1, number of averages = 2. For each gradient combination, the total acquisition time was approximately 7 min, reaching a total DDE data acquisition of $\sim$ 1h20 min.

2.7. Diffusion data pre-processing

For consistency, the same diffusion data pre-processing steps were performed on both *in vivo* and *ex vivo* datasets. Before starting the diffusion data analysis, masks for delineation were manually drawn slice-by-slice using Matlab (Matlab R2018b). All datasets were corrected for Gibbs ringing artifacts (Kellner et al., 2016; Henriques, 2018) in Python (Dipy, version 1.0 (Garyfallidis et al., 2014)) which suppresses the Gibbs oscillations effects based on subvoxel Fourier shifts (total variance analysis across three adjacent points for each voxel used to access Gibbs oscillation suppression). All diffusion-weighted datasets underwent realignment via a sub-pixel registration method (Guizar-Sicairos et al., 2008) in which each set of data for every total diffusion b-value would be realigned to a counter defined dataset with similar DDE gradient pattern combinations and adjacent lower b-value.

2.8. CTI reconstruction

CTI was then directly fitted to the data using a linear-least squares fitting procedure implemented to the following equation (Henriques et al., 2020):

$$
\begin{aligned}
\log E_\Delta(q_1, q_2) = &-(q_{1i}, q_{1j} + q_{2i}, q_{2j})\Delta D_{ij} \\
&+ \frac{1}{6}(q_{1i}q_{1j}q_{1k}q_{1l} + q_{2i}q_{2j}q_{2k}q_{2l})\Delta^2 \overline{D}^2 W_{ijkl} \\
&+ q_{1i}q_{1j}q_{2k}q_{2l}\Delta^2 C_{ijkl} + O(q^6)
\end{aligned}
\tag{1}
$$

where D_{ij}, W_{ijkl} and C_{ijkl} correspond to the diffusion, kurtosis and covariance tensors, respectively (and the covariance tensor is justified for DDE at long mixing times, when the Z_{ijkl} tensor approaches C_{ijkl}). The sources of kurtosis can be extracted from these tensors in the following way (Henriques et al., 2020): 1) the total kurtosis K_T can be computed from W_{ijkl}; 2) the two inter-compartmental kurtosis sources (K_{aniso} and K_{iso}) can be extracted from C_{ijkl}; and 3) the microscopic kurtosis source μK is then given simply by $\mu K = K_T - K_{aniso} - K_{iso}$.

2.9. Region of interest analysis

A Region of Interest (ROI) analysis was performed by manual selection of ROIs in the ipsilateral hemisphere and selection of symmetric ROIs in the contralateral regions for every dMRI estimate (MD, K_T, μK, K_{iso} and K_{aniso}). This ROI selection was carefully performed slice by slice in all brains (Supplementary Fig. S7). Within these more general ROIs, gray matter (GM) and white matter (WM) regions were further selected according to a manual selection of WM regions based on an anatomical brain map (Franklin and Paxinos, 2019) combined with FA contrasts. All ROI analyses were performed in Matlab® ver. R2018b (MathWorks, Natick, MA, USA).

2.10. Interhemispheric ratio analysis

An interhemispheric ratio analysis was performed by calculating interhemispheric ratios (percentage changes) between ipsilesional and contralesional (stroked brain) hemispheres ($N = 10$ *ex vivo* and $N = 5$ *in vivo*) via:

$$
Ratio(\%) = \left(\frac{Par_{ipsi} - Par_{contra}}{Par_{contra}} \times 100 \right)
\tag{2}
$$

where Ratio(%) is the interhemispheric ratio of parameters, Par_{ipsi} is a CTI-driven parameter (MD, K_T, K_{aniso}, K_{iso}, and μK) on the ipsilesional side, and Par_{contra} is the same parameter on the contralesional side.

2.11. Statistical analysis

A Shapiro-Wilk test was used to test normality ($p < 0.05$) over the hemispheric ratio data for all affected voxels, GM and WM, for both *ex vivo* and *in vivo* data. Upon normality validation, a one-way ANOVA test ($p < 0.05$) was performed to test if the interhemispheric mean differences were significant between the different metrics (MD, K_T, μK, K_{iso} and K_{aniso}) for total affected voxels, WM and GM data, with a subsequent Tukey's HSD multiple comparison test to assess which metrics means were statistically significant ($p < 0.05$).

The differences between the ROI average values of all absolute diffusion metrics in ipsilesional and contralateral hemispheres were tested using paired t-tests, accounting for multiple comparisons (15 comparisons) using Bonferroni corrections (Supplementary Fig. S10 and S11). All statistical analysis were performed in Matlab®.

2.12. Data visualization

All volumetric datasets were rendered with ImageJ. Volume render maps were produced using the plugin Volume Viewer (Barthel, 2012), with tricubic smooth interpolation for K_T and μK sources. MRIcroGL (Rorden and Brett, 2000) was used to create 2D lesion overlay maps on the averaged $b = 0$ s/mm^2 images. NIFTI format images from each metric affected voxels ROI (GM + WM) and respective estimates were overlaid.

2.13. Nissl Cresyl Violet staining

Histological analysis was performed in one of the stroked *ex vivo* samples. Slices were obtained through Vibratome sectioning with a thickness of 0.04 mm and Mowiol containing 2.5% 1,4 diazobicyclo[2.2.2]-octane (DABCO, Sigma, D2522) was used as the mounting media. The brain sections were then fixed with 10% formalin and processed with Nissl-Cresyl Violet staining for microscopy in order to assess tissue damage and cell loss within the infarcted region.

2.14. Optical imaging

Histological imaging was performed with a ZEISS Axio Scan.Z1 (Zeiss, Germany) coupled to a Hitachi 3 CCD color camera and processed with QuPath 0.2.3 (Fig. 3E). Images were magnified (×53) for both ipsi- and contralesional hemispheres.

3. Results

3.1. Simulations

We begin by attempting to predict how neurite beading and other stroke hallmarks would be expressed in CTI metrics. Fig. 2A examines how different degrees of beading (increasing cross-sectional variance) affects all metrics derived from CTI. Interestingly, we find direct signatures for increased beading effects in CTI-driven signals. In particular, we find large μK increases accompanied by small decreases in K_{aniso} as the beading degree increases. In these simulations, K_{iso} remains zero for all beaded scenarios by definition. Consistent with Budde et al. (Budde and Frank, 2010), we also find concomitant decreases in MD.

We then investigate the scenario of edema formation (c.f. Fig. 2B), by adding a free water component to a beaded system (in this case, the strongest beading scenario showin in Fig. 2A). As the edema fraction increases (from only beads (no edema) to only free water (only edema), $0 < f_{edema} < 1$), μK and K_{aniso} decrease in value, in a similar fashion, while MD increases and total kurtosis decreases. In this case, K_{iso} exhibits a peak – it first increases as the diffusivity difference between the beads and the more freely diffusing water is initially large, but as the free water fraction begins to dominate, the variance in diffusivities is

strongly skewed to free diffusion, culminating in totally free diffusion (no beading, $f_{edema} = 1$), which has zero variance ($K_{iso} = 0$).

Finally, we consider edema formation, but rather than in a beading scenario, we inspect it in the context of "swelling" of disconnected, large spherical objects (e.g., representing quasi-spherical cell swelling, Fig. 2C). In this case, K_{aniso} remains constant while K_T and K_{iso} evidence maxima as the edema fraction increases, followed by a decline in the metrics with increasing edema as the system reaches a "cyst" stage – only a single Gaussian component with free water diffusivity. Importantly, for this scenario, μK is negative, and it approaches zero as the edema fraction increases. Hence, within the scope of these simulations, CTI provides differential signatures for beading, edema, and cell-swelling effects.

While these simulations represent relatively simplistic scenarios, we further attempted to increase the level of complexity and investigate how diffusion in the extracellular space could affect the CTI metrics. In particular, Figs. S1–S3 show these simulations for three different values of the extracellular diffusivity. Strikingly, according to these simulations, the extracellular space diffusion in beaded scenarios can increase the isotropic kurtosis, especially if the extracellular diffusivity is high (Fig. S3) but otherwise the trends for varying cross-sectional variance reported above for μK and K_{aniso} remain intact, even though small baseline shifts may be incurred depending on the extracellular diffusivity value. In summary, these Monte Carlo simulations of more complex scenarios still point to the sensitivity of CTI metrics to increased cross-sectional variance and edema effects.

3.2. Focal thrombi induction

The experimental part of this work sought to measure the kurtosis sources, for the first time, in stroke. First, we validated that ischemic lesions were induced reproducibly in the mice. Indeed, upon injection with a photosensitive dye and irradiation with the appropriate wavelength (Fig. 1F) for generation of reactive oxygen species, severe endothelial damage and thrombi formation are expected (Watson et al., 1985). Correspondingly, a well-delineated extensive unilateral lesion in T_2 weighted images (Fig. 3A) appeared 3 h post-ischemia, with strong hyperintense contrast, unilaterally covering the barrel cortex and to some extent the hippocampus. The dMRI signals averaged across all acquired directions (powder-averaged (Jespersen et al., 2013)) also clearly delineated the stroke area as hyperintense signals (Fig. 3B). For all $N = 15$ mice that underwent ischemic induction, the stroke location and general features were highly reproducible (c.f. Supplementary Fig. S4, which depicts five representative strokes *ex vivo*). By contrast, no interhemispheric differences could be observed in the sham group ($N = 5$ mice injected with the photosensitive dye but that did not undergo irradiation (Fig. 3C, D)). In this group, both T2-weighted images and powder-averaged diffusion-weighted images appear symmetric and without abnormal contrasts.

A histological evaluation of the stroked area (Fig. 3E) clearly demonstrated abnormalities in Nissl (Cresyl violet) staining. The zoomed view of the ipsilesional cortex (Fig. 3E, right) also shows the reduced staining and density, compared with the contralesional cortex (Fig. 3E, left).

3.3. Conventional total kurtosis and mean diffusivity in stroke

The signal to noise in the *ex vivo* CTI experiments was high (70 ± 25 at $b = 0$ s/mm^2), and very few, if any, artifacts could be observed in videos of the entire data (c.f. Supplementary Video 1 for a representative example). As in prior studies (Hui et al., 2012; Umesh Rudrapatna et al., 2014), total kurtosis was much higher in the stroked group. Fig. 4A (first row) shows the elevated K_T in a representative mouse brain in the affected hemisphere, as well as reduced MD and slightly reduced FA (Supplementary Fig. S5). The K_T values appeared elevated in both GM and WM, and its contrast was more conspicuous compared with the MD contrast. On the other hand, no interhemispheric differences
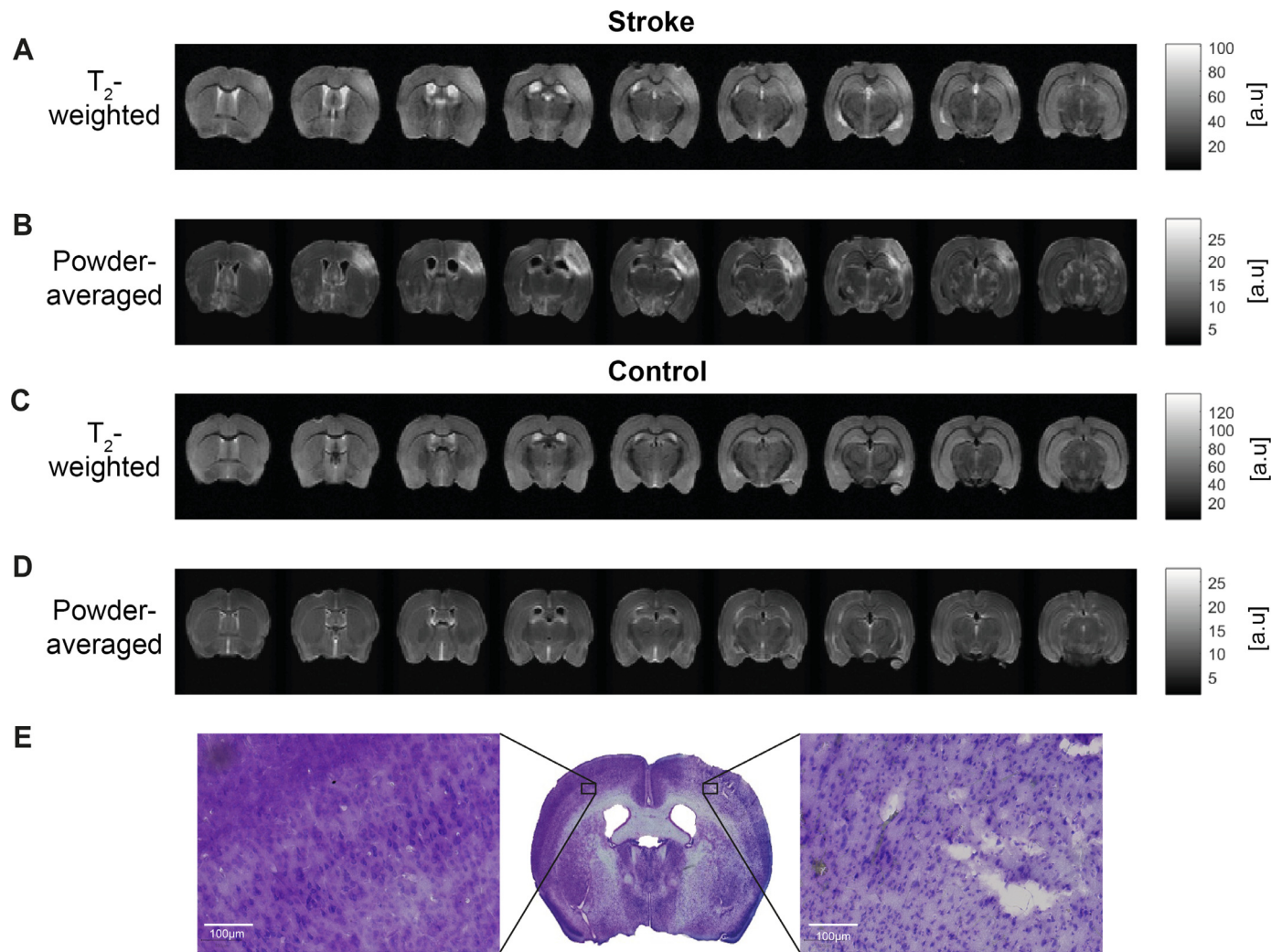
Fig. 3. Raw T2-weighted, powder-averaged diffusion-weighted data and histological validation of the lesion. (A, C) T2-weighted images and (B, D) the powder-averaged signal decays computed by averaging the diffusion-weighted signals decays over 135 directions of diffusion wave vectors from representative extracted brains from both stroke ($N = 10$) and sham ($N = 5$) groups (total b-value = 3000 s/mm^2), respectively. Nine representative coronal slices are presented from rostral to caudal direction. The T2-weighted contrast shows elevated intensity around the infarcted region (left hemisphere, barrel cortex) GM, whereas the powder-averaged contrast presents elevated values for both GM and WM within the infarcted region. (E) Histological analysis was performed to assess cell damage and validate the presence of a lesion using cresyl violet staining. A clear lesion was noted in the left cortex and subcortical region 3 h post-ischemia ×53 magnification) associated with micro vacuolation of the cytoplasm, and fewer intact cells associated with cell damage, when compared to the intact contralesional region (left).

were observed in K_T in the control group (c.f. Fig. 4B, first row, for a representative control brain), and other diffusion tensor metrics (MD, FA) were also symmetric. However, it is difficult to draw conclusions on the sources for these stroke-induced changes in K_T or MD which could involve any of the scenarios described in Fig. 1A, as also represented in the illustration of kurtosis sources (Fig. 4C, first row).

3.4. CTI-derived microscopic kurtosis source (μK)

The μK metric derived from the CTI analysis in the stroked brains – which represents contributions from cross-sectional variance and/or restricted diffusion – was dramatically elevated in the affected area (Fig. 4A, second row). This observation was consistent for all $N = 10$ *ex vivo* brains and $N = 5$ *in vivo* mice (c.f. Supplementary Figs. S6 and S9 for 5 representative depictions, evidencing this high reproducibility), and a visual examination shows that the elevated μK appeared higher both in GM and WM tissues. The visual appearance of the stroke in the μK maps, especially vis-à-vis contrast compared to the contralateral hemisphere, was striking. In the control group, again the μK maps showed

no striking interhemispheric differences (Fig. 4B, second row), suggesting that the elevated μK observed in stroke (Fig. 4C, second row) is due to tissue properties rather than, e.g., arising from some asymmetric left-right (or other) imaging artifact. The control findings are also consistent with those previously found in Henriques et al. (2021a, 2021b), using a similar CTI pulse sequence.

3.5. CTI-derived isotropic kurtosis source (K_{iso})

The isotropic kurtosis contrast, which represents the variance in diffusion tensor traces in the tissue derived from CTI analysis exhibited increases upon ischemia at the 3 h time point, mainly in WM, and much less in GM (Fig. 4A, third row). No apparent differences in WM or GM tissues were observed between hemispheres for K_{iso} in the control group (Fig. 4B, third row), suggesting that the variance in isotropic tensor magnitudes (Fig. 4C, third row) in the stroked group again cannot be related to imaging artifacts.
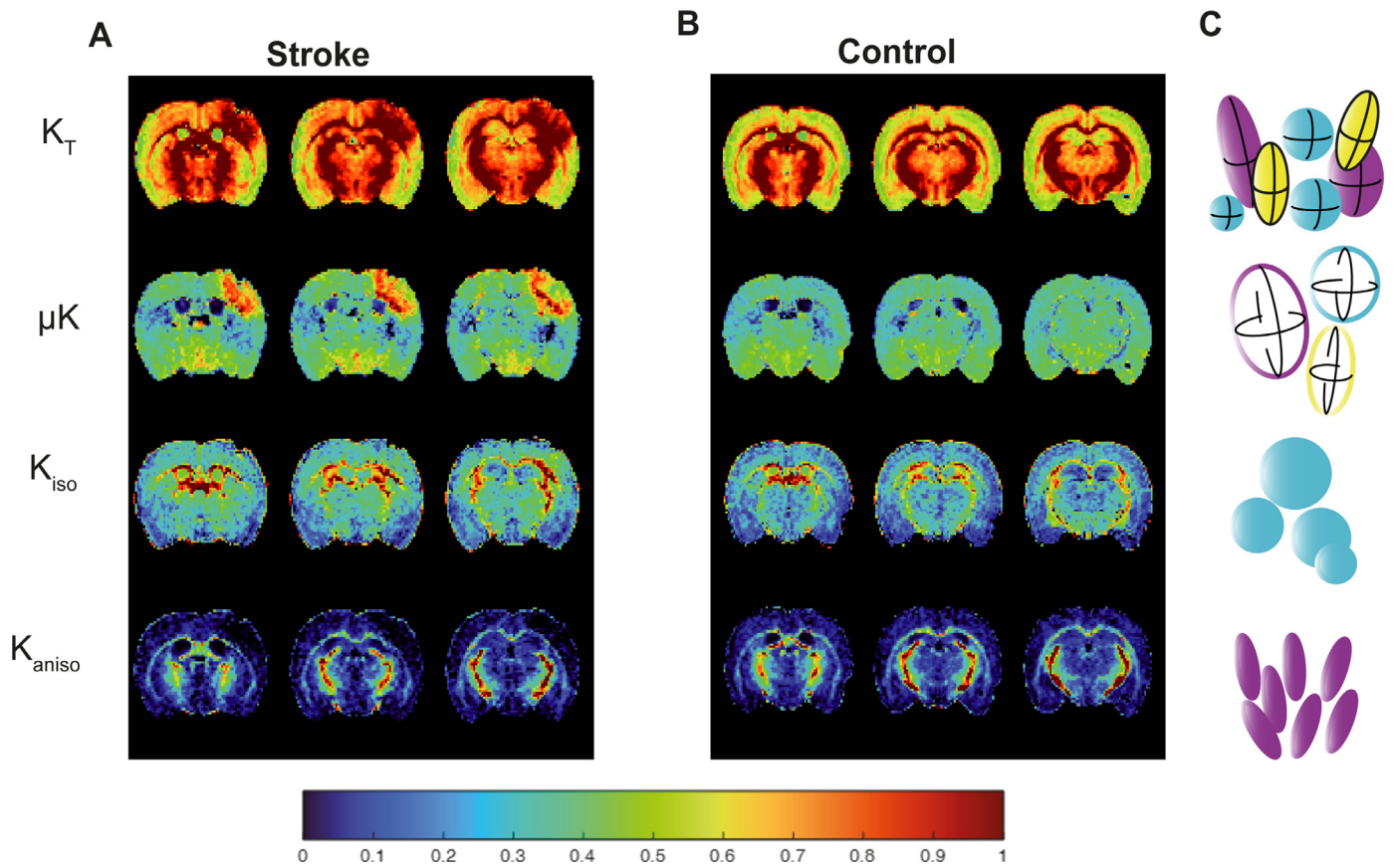
Fig. 4. Kurtosis sources maps from the ex vivo experiments for representative stroked and control brains. (A, B) Total kurtosis and kurtosis source maps: (first row) K_T, (second row) μK, (third row) K_{iso} and (fourth row) K_{aniso}) for three slices from representative brains from (A) stroke and (B) control groups. (C) Respective illustration of each kurtosis source. In the ischemic group ($N = 10$), the ipsilesional hemisphere shows higher K_T mainly in GM. A clearer distinction between hemispheres is observed in μK, with larger μK values in both WM and GM. K_{aniso} is lower in both WM and GM within the ipsilesional hemisphere when compared to the contralesional hemisphere. No asymmetries or other artifacts were noted for the sham group ($N = 5$).

3.6. CTI-derived anisotropic kurtosis source (K_{aniso})

The anisotropic kurtosis contrast in stroke, which is proportional to the degree of microscopic anisotropy, irrespective of orientation dispersion, exhibited large decreases in K_{aniso}. The decreases were more evident in the ipsilesional GM (Fig. 4A, fourth row) but WM values also exhibited some decreases. In the control group, the same K_{aniso} contrast did not appear different between the hemispheres (Fig. 4B, fourth row). In other words, stroked GM was characterized by decreased microscopic anisotropy (Fig. 4C, fourth row).

3.7. Quantitative analysis of the ex vivo group

We analysed the percent changes for all affected voxels (GM and WM combined as well as for GM and WM separately). Fig. 5A shows the magnitude of the effects with respect to the contralesional hemisphere in the stroked group. While total kurtosis changes by ~50% of its control value in stroke, the μK contrast in GM+WM was nearly double, with ~80% changes. While K_T changes were quite similar between GM and WM, the μK changed more dramatically in WM (~120%) and still very strongly in GM (~70%). K_{iso} on the other hand, changed by ~65% in general, with higher affinity to WM (~80% change but with large standard error). Finally, K_{aniso} decreased by over 70% overall, with nearly ~−70% changes in GM and ~−50% changes in WM. The corroborative effect size results, shown in Supplementary Fig. S10, report significant K_T, μK and K_{aniso} interhemispheric differences in GM ($p < 0.05$) as well as K_T ($p < 0.05$) and μK ($p < 0.01$) differences in WM.

Since μK maps are generally noisier than K_T maps due to the subtraction used in CTI methodology, the effect size should be considered in terms of the respective "contrast to noise", or size of the effect over the standard deviation of the effect. In the entire lesion, the median $\pm$ SD for K_T and μK effects (across animals) were 1.13 ± 0.12 and 0.72 ± 0.08, respectively, leading to similar ratios of 9.3 and 8.6, respectively, suggesting a similar detection power for both metrics.

We then assessed the overlap of CTI metrics with their more conventional counterparts by overlaying the different areas found to be affected by each metric (Fig. 5B). The ensuing overlay analysis clearly demonstrates that μK detects more affected voxels overall, including in the lesion periphery, with a higher affinity towards GM; areas with large overlap between the sources indicates multitude microstructural effects, while areas characterized solely by μK represent more subtle effects on the tissue. Areas with large K_{iso} and μK overlap appear more confined to the core of the stroke. Supplementary Fig. S8 shows that these observations are highly consistent n the other animals.

3.8. In vivo CTI in stroke

To ensure that the effects above were not dominated by fixation effects upon perfusion of the brains (Thelwall et al., 2006), and to show the feasibility of the CTI approach in vivo, we repeated the same CTI experiments at the 3 h time point post-ischemia in vivo. Supplementary Video S2 shows the data, with very little (if any) artifacts following preprocessing, and the typical signal to noise in these experiments was 45 ± 11. Fig. 6 shows the CTI results in the ischemic brain in vivo for a
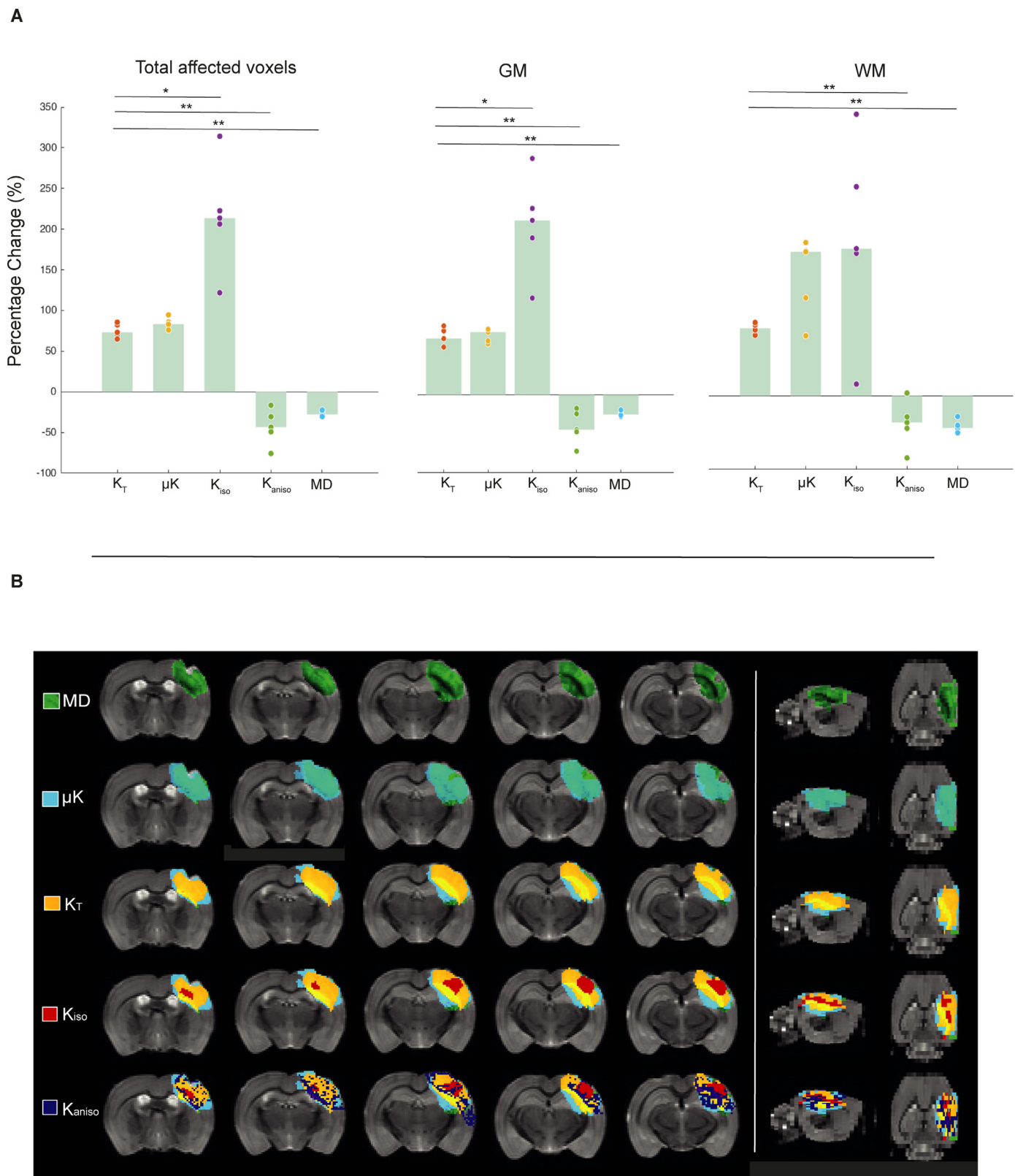
A

B

Fig. 5. Interhemispheric percent change and ipsilesional (A) and MD / kurtosis / kurtosis source map overlays in affected voxels (B). (A) Ipsilesional-contralesional ratios accounting for the mean of all voxels for different ROIs – GM and WM – from ten stroked brains ($N = 10$) were assessed for K_T, μK, K_{iso}, K_{aniso} and MD. Median values are presented for total affected voxels, GM and WM. μK percentage change was distinctly more elevated for both GM and WM. Statistically significant differences ($p < 0.05$) were found between the ratios of K_T and μK in all affected voxels, as well as between K_T, μK, K_{iso} and K_{aniso} and MD in both GM and WM, and total affected voxels; (B) Metrics overlay analysis using MRIcroGL using the b_0 averaged images of a representative stroked brain as background. 2D renderings of overlay ROI maps on the ipsilesional hemisphere were performed according to the number of voxels affected by the lesion in each metric. Metrics in the ROIs were overlayed by the following order: MD (green), μK (cyan), K_T (yellow), K_{iso} (red) and K_{aniso} (dark purple). Coronal slices are presented, showing that μK highlights a greater area than MD for affected voxels, followed by K_T, K_{iso} and K_{aniso}. On the right, the sagittal (left hemisphere) and axial views presenting the lesioned region are displayed following the same order of ROI and estimates overlay.
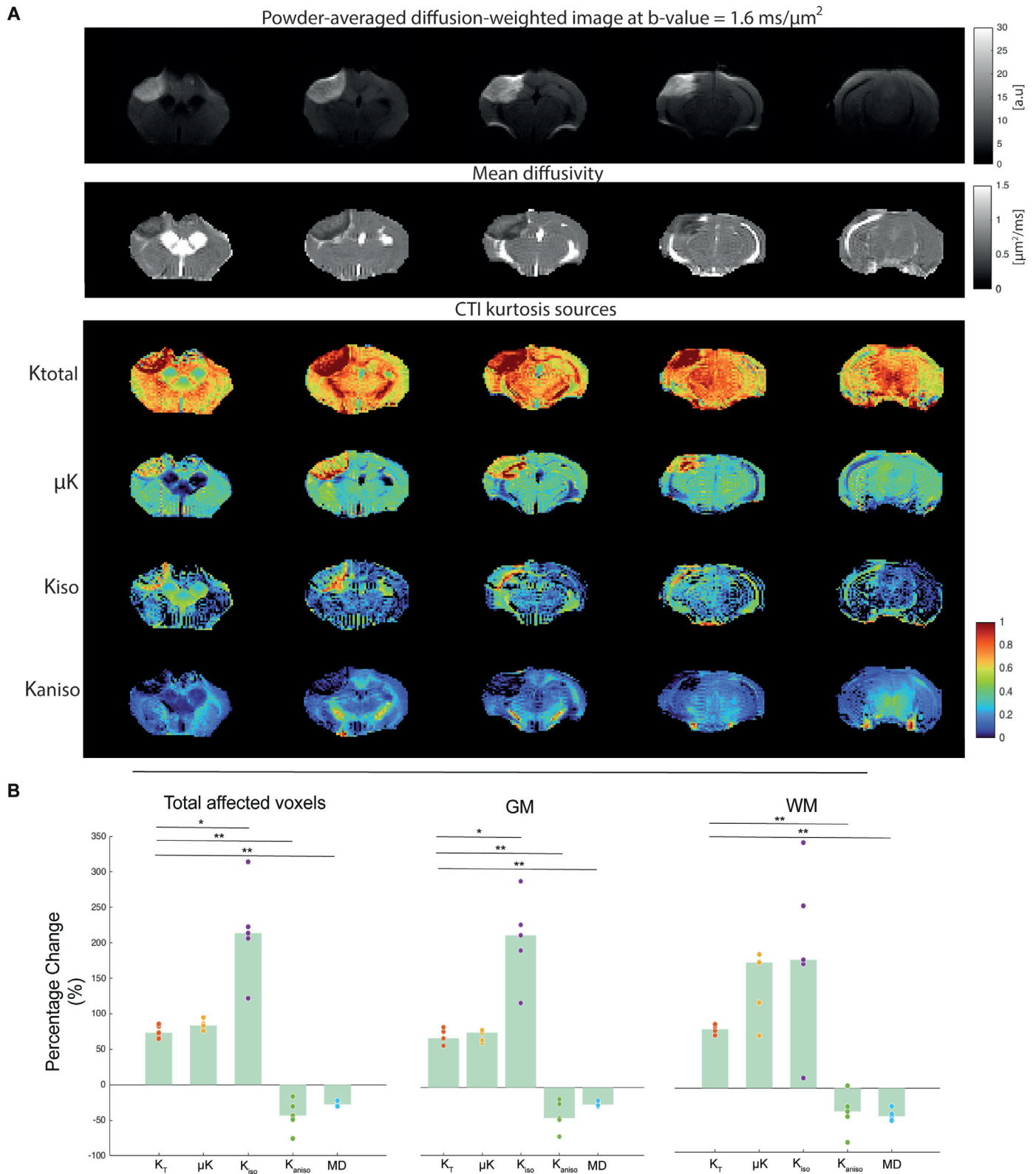
Fig. 6. *In vivo* CTI in the 3 h time point post-ischemia. (A) Powder-averaged diffusion-weighted image at b-value = 1.6 ms/μm^2 of a representative animal scanned *in vivo* 3 h post ischemic onset (first row) and respective MD (μm^2/ms) and kurtosis sources map. In the stroked animal, K$_T$ is higher in the lesion area, consistent with the *ex vivo* maps. μK maps reveal much higher values in the lesioned region compared with the ipsilesional hemisphere, for both white and gray matter. K$_{iso}$ is elevated in white matter and K$_{aniso}$ is lower within the lesioned region (both white and gray matter). (B) Ipsilesional-contralesional ratios accounting for the mean of all voxels for different ROIs – GM and WM – from the five stroked *in vivo* animals ($N = 5$) for K$_T$, μK, K$_{iso}$, K$_{aniso}$ and MD. Median values are presented for total affected voxels, GM and WM. Percentage change was distinctly higher for both GM and WM in K$_{iso}$. Statistically significant differences ($p < 0.01$) were found between the ratios of K$_T$, μK, K$_{iso}$ and K$_{aniso}$ and MD in both GM and WM.

representative mouse. Fig. 6A shows the raw powder averaged CTI data (Fig. 6A, top row) and the ensuing MD maps (Fig. 6A, second row), both evidencing the stroked area very clearly. The following rows depict the total kurtosis and the three different kurtosis sources extracted from the CTI methodology. The same trends as observed in the *ex vivo* results persist for the *in vivo* scenario, with minor variations. First, as in the *ex vivo* data, μK increases significantly at this time point, and is accompanied by a decreased K_{aniso}. Interestingly, we find somewhat higher values of K_{iso} in the stroked area *in vivo*, likely reflecting more edema under this condition. Furthermore, the dramatic elevation of μK persists in both GM and WM, while K_{iso} is more clearly higher in WM. K_{aniso} decreases more prominently in GM, consistent with the *ex vivo* trends reported above.

Upon quantification (Fig. 6B) most of these trends exhibit statistical significance when the ipsilesional hemisphere is compared with the contralesional hemisphere.

4. Discussion

Micro-architectural modulations accompany a multitude of biological processes ranging from learning (Scholz et al., 2009), development (Suter and Jaworski, 2019) and plasticity (Hughes et al., 2018) to aging (Hill et al., 2018), and they are particularly relevant in neurodegeneration and neural injury (Murphy and Corbett, 2009). In stroke, diffusion MRI and particularly DWI and DTI have played a crucial role in early detection and evaluation of the lesion (Moseley et al., 1990a, 1990b; Mukherjee, 2005; Hui et al., 2012; Umesh Rudrapatna et al., 2014) and enhanced sensitivity was reported for DKI (Hui et al., 2012; Umesh Rudrapatna et al., 2014); however, specificity remained inherently limited due to the conflation of different microstructural features within the estimated parameters (Henriques et al., 2020, ,2021b).

Here, we harnessed Correlation Tensor MRI (Henriques et al., 2020, ,2021b) to disentangle the contributions of the different diffusional kurtosis source in ischemia, both *ex vivo* where imaging can be performed with very high signal to noise and resolution, and without potential limiting effects due to motion and physiological stability, as well as *in vivo* under more realistic conditions. The CTI methodology enhances specificity towards the underlying kurtosis sources by making the 4th order correlation tensor *Z* (Jespersen and Buhl, 2011, Jespersen, 2012; Jespersen et al., 2013) which approaches the covariance tensor *C* at long mixing times, accessible from the DDE signals. By measuring the total kurtosis as well as *C*, it becomes possible to quantify the anisotropic, isotropic and microscopic kurtosis contributions to the total kurtosis while also quantifying the more conventional MD, K_T, and FA metrics typically derived from conventional DKI. In this study, we posited that the CTI approach can enhance specificity (and perhaps sensitivity) and thereby potentially provide insights into the underlying pathophysiology in the ischemic tissue.

The 3 h timepoint in the Rose Bengal stroke model used in this study can be considered "subacute" due to the endothelial damage caused by the photosensitive dye (Dietrich et al., 1987; Stoll et al., 2008; Piao et al., 2009). In this subacute phase, at least three major microarchitectural modulations occur downstream of the disruption in oxygen supply (Hossmann, 2006): in particular, (1) neurite beading (Budde and Frank, 2010; Kislin et al., 2017) due to neuronal dysfunction (Hori and Carpenter, 1994; Takeuchi et al., 2005; Enright et al., 2007; Kislin et al., 2017); (2) edema formation (Stokum et al., 2016) (more free water in the tissue) and disruption of extracellular/intracellular ionic balance; and (3) cell swelling (Xing et al., 2012) (enlargement of cell body structures). In the past, decreases in MD and increases in K_T were considered to reflect beading effects (Budde and Frank, 2010; Skinner et al., 2015). However, increases in total kurtosis can arise from multiple scenarios, while MD decreases can also arise from other effects such as shrinkage of relevant length scales in the tissue. Importantly, previous experiments harnessing the enhanced sensitivity of Oscillating Gradient Spin Echo (OGSE) to (sub)cellular length scales provided similar evidence point-

ing towards changes in microstructure over different length scales along the time course of ischemia (Wu et al., 2014, 2019), and recent OGSE studies have shown enhanced total kurtosis contrast in ischemia when different diffusion times were probed (Wu et al., 2018). Therefore, perhaps the most interesting finding of this study, is that CTI metrics can provide enhanced specificity and insight into these scenarios.

Perhaps most importantly, we find that increases in $\mu K > 0$, coupled with the decreases in K_{aniso}, could be considered a hallmark of increasing cross-sectional variance, which we here interpret, according to our simulations, as arising at least in part from beading effects in small, microscopic-scale structures (Fig. 2A). Interestingly, signal from extracellular space does not change the overall direction in the CTI metrics (Fig. S1–S3) albeit small baseline shifts incurred by extracellular diffusion. Therefore, according to these simple simulations, the extracellular space acts more as a Gaussian component (consistent with Skinner et al.'s findings (Skinner et al., 2015)), while the cross-sectional variance occurring in the "intraneurite" space is more consistent with our μK observations. This further lends credence to the simulations shown in Fig. 2B, C which only consider the addition of the edema component as a simple Gaussian diffusion fraction. Our experimental findings were consistent with these predictions, evidencing a very large $\mu K > 0$ increase, coupled with a decrease of K_{aniso} to nearly zero, both *ex vivo* and *in vivo* (Figs. 5A and 6B). Interestingly, our simulations suggest that the combination of μK, K_{aniso} and K_{iso} can also differentiate between the scenarios of swelling of larger spherical structures (e.g., cell bodies) and beading of small structures (dendrites, axons), given that for larger spherical structures, a $\mu K < 0$ is predicted for sufficiently long diffusion time due to confinement. This behavior is expected to be diffusion time- (and perhaps mixing-time-) dependent, but at least under the experimental conditions executed here, the μK measurements seem to be more sensitive to the cross-sectional variance effects in small structures, even when extracellular space is considered (Fig. S1–S3).

Importantly, the observation of beading effects in axons (Baltan, 2014) were later generalized to other neural tissue components, including dendrites and neurites, suggesting the phenomenon occurs within a significant volume in the tissue (Kislin et al., 2017). In some cases, these beading effects were shown to further be related to mitochondrial microstructure, which upon ischemia also evidences beading phenomena within the dendrites, on a similar scale as the dendrite beading itself (Kislin et al., 2017). In these studies, the extent of beading observed by 2-photon microscopy was found to vary with severity of injury and in some cases, it was reversible. Therefore, it is plausible that CTI-driven mapping of μK, coupled with better correlations with dendrite beading effects, could impart specificity towards these important pathophysiological effects. Thus, it can be hypothesized that μK could potentially better reflect the extent of the ongoing damage in the tissue. This also provides an opportunity to follow these effects over time and offer a better characterization of the lesion progression and ultimately, it may be considered as a potential marker of functional outcomes. Future longitudinal CTI experiments in stroke will be required to establish the time course of its parameters and their correlations with functional outcomes; similarly, more advanced simulations considering more complex microstructural scenarios are warranted to better elucidate the nature of μK under ischemic (or other) conditions. While such experiments are ongoing and will be reported in due course, this study at least suggests that these are important avenues for future investigation.

Importantly, we also find CTI signatures for the scenario of edema formation (c.f. Fig. 2B): when edema fraction increases (from only beads to only free water, $0 < f_{edema} < 1$), μK and K_{aniso} decreases in a similar fashion, while MD increases and total kurtosis decreases. In this case, K_{iso} first increases as the diffusivity difference between the beads and the more freely diffusing water is initially large but as the free fraction begins to dominate, the variance in diffusivities is strongly skewed toward free diffusion, culminating in totally free diffusion, which has zero tensor magnitude variance ($K_{iso} = 0$). Finally, if we consider edema forma-

tion in the presence of "swelling" of disconnected relatively large spherical objects (e.g., cell bodies), Fig. 2C), K_{aniso} remains constant (at zero) while K_T and K_{iso} evidence maxima in their values; more importantly, this case also contains a "signature": μK for these scenarios is negative and increasing towards zero as edema fraction increases. In our study, K_{iso} increases were much more prominent *in vivo*, likely because edema components could be drained by the fixation process. In addition, the K_{iso} changes are greater in white matter because the overall diffusivity in normal WM is small, and since K_{iso} is expected to be larger when the difference in the diffusivities of the different components increases. In other words, as edema forms in WM, the difference between the edema diffusivity and WM diffusivity is larger than the difference between GM diffusivity and edema diffusivity, making K_{iso} larger for the scenario of edema+WM. Finally, on-going neuroinflammation which can begin to occur at the 3 h time point (Buscemi et al., 2019) may also change K_{iso} as it could potentially contribute yet another diffusivity to the system.

We note that in terms of sensitivity, although the percent changes observed in μK are much larger than K_T (likely because K_T is proportional to the sum of two increasing terms μK and K_{iso}, and one *decreasing* term K_{aniso}, making its overall increase magnitude smaller), μK is also a noisier metric by definition. The effect size across animals is shown in Figs S10 and S11 for *ex vivo* and *in vivo* conditions, respectively; a calculation of the median+/-iqr of μK and K_T which provides at least an indication of the effect size relative to the noise of the measurement, suggests that μK is at least as sensitive as K_T, witheffect sizes of ~9.3 vs. ~8.6, respectively. However, given that the percent change is so much larger for μK, lesions may be more easily identifiable and delineated using this metric. It may be interesting to perform test-retest of the metrics in the future to determine whether μK would be potentially more sensitive than its K_T counterpart.

Our findings also have several implications for dMRI modeling in health and disease. First, the often-ignored μK (Ozarslan et al., 2016; Szczepankiewicz et al., 2016) (as well as diffusion time-dependent effects Jespersen et al., 2019) is clearly a confounding factor in existing "tensor valued" modeling and analyses (Eriksson et al., 2013; Szczepankiewicz et al., 2016). Finite μK contribution could clearly bias kurtosis source metrics (Henriques et al., 2021b) and its own contrast – as here shown – could be important when investigating microstructural changes e.g. upon neurodegeneration or neural injury. Ignoring μK in the analyses can conflate the other kurtosis sources in complicated ways (Henriques et al., 2021b); this in turn could mislead the interpretation of the observed changes in micro-architecture.

As in every study, we recognize several important limitations and future perspectives arising from this current work. First, the CTI pulse sequence relies on a DDE pulse sequence, which is less available under clinical conditions, making its clinical applicability less immediate. In addition, in this study we have used long and comprehensive CTI acquisitions, which provide all the kurtosis sources simultaneously but whose length could be prohibitive in the clinic. Still, DDE acquisitions have been achieved on clinical systems in the past (Lawrenz and Finsterbusch, 2013; Yang et al., 2017; Novello et al., 2021), and it is important to note that the CTI acquisitions can be considerably shortened. Acceleration could be achieved by reducing the number of applied directions. In addition, specific kurtosis sources can be extracted from subsets of the CTI acquisitions, thereby enabling a further shortening of the total acquisition time.

Second, CTI does not rely on any explicit assumptions other than (i) the verifiable (and here verified) long mixing time regime and (ii) negligible exchange. The timing of the sequence (10 ms diffusion time and 10 ms mixing time) suggests that exchange effects (Kärger, 1985; Åslund et al., 2009; Lampinen et al., 2017) are likely small on this timescale (Nilsson et al., 2013; Obata et al., 2018). However, we cannot deconfound exchange completely at this point as a potential modulator of the magnitude of the different CTI metrics. For example, in the stroked tissue, the membrane depolarization following the ischemic cascade can lead to changes in its permeability. We expect that μK will re-

flect exchange at least to some extent and exchange should also greatly modulate K_{iso} since, for example, for a system of two different diffusion coefficients with exchange, K_{iso} approaches zero in the limit of fast exchange and is larger for negligible exchange. Interestingly, in our study, μK is much higher than K_{iso} upon stroke (Figs. S10 and S11), which may point to a dominance of cross-sectional variance effects in small objects (neurite beading). Extensive future studies investigating Monte Carlo simulations of exchange under beading scenarios with CTI, as well as theoretical and experimental studies on its diffusion- and mixing-time dependencies, will be required to establish the specific contributions of specific microstructural effects and exchange to the CTI contrasts.

A third limitation involves the Rose-Bengal stroke model used in this study, which is known to produce a limited extent of penumbra (Walz, 2016). We expect that future studies comparing the CTI results in this study with more clinically relevant stroke models such as the Middle Cerebral Artery Occlusion (MCAO) model (Pitts et al., 1986), will shed much light into how CTI can assist in measuring penumbra. The characterization of penumbra (Astrup et al., 1981) is a major goal for stroke imaging given the interest in understanding the tissue state at any given time. However, the conflation of microstructural effects in MD or K_T make the penumbra characterization more difficult. We expect that mapping μK, K_{iso} and K_{aniso} over the time course of ischemia could already provide insight into the tissue state. Furthermore, it is conceivable that mismatches between the different CTI metrics could be plotted (Fig. 5B) and perhaps even contrasted with, e.g., measurements of perfusion, to quantify the penumbra and the core more comprehensively. We note that if μK reflects cross-sectional variance due to dendrite beading and mitochondrial damage (or even if its magnitude reflects exchange and thus more permeable membranes due to the ischemic cascade), then it could be envisioned that μK increases (coupled with K_{aniso} decreases) would better reflect the ongoing damage in the lesion core, and as such perhaps could better indicate the tissue status compared to the conflated counterparts MD or K_T. Similarly, assuming that K_{iso} better reflects edema, it may indicate on the extent of salvageable penumbra. Further studies on animal models that produce only edema (e.g. (Le Bras, 2020) could shed light into the specificity of this metric.

Fourth, our *ex vivo* results may be more prone to fixation effects (Thelwall et al., 2006), although they also enable a robust and reliable estimation of parameters. However, our *in vivo* results revealed high consistency between the two conditions, with slightly more edema *in vivo* as reflected by increased K_{iso}. The definition of the 3 hour time point post-ischemia may have been slightly temporally "blurred" in the *in vivo* group by the ~1h20m acquisition time, however, since we acquired the shells separately it was possible to compare partial results during the entire acquisition time, and we find only very minor – if any at all – differences in the kurtosis sources between 3h and 4.5 h (data not shown). Clearly, future studies should target the entire time course of ischemic progression, from acute to subacute to chronic phases and include behavioural metrics, neurological scores, and quantifiable end-point histology; indeed, the histological study here was performed only to verify that the stroke was successful, and not to quantify the extent of beading or edema. Future studies should attempt to correlate CTI metrics with more quantitative histology to elucidate the correlation between CTI parameters, stroke severity, and potential for recovery. Such experiments are ongoing and will be reported in due course.

We also note that the simulations in this study were designed to highlight general features, rather than to represent a full exploration of the large parameter space. Future work should aim to explore both larger parameter spaces (Budde and Frank, 2010; Skinner et al., 2015; Callaghan et al., 2020) and potentially more realistic neural substrates, to correlate CTI signals, time-dependence effects and the specificity to beading, swelling, edema and exchange, as well as explore more scenarios of packing and extracellular space. Still, the extracellular space simulations provided here provide confidence that the general trend of the effects holds, even if with small amplitude modulations due to the

specifics of the simulation parameters chosen (which also makes it possible to potentially use these methods to model intra/extra-cellular space and potentially fit them from the data).

Finally, the CTI pulse sequence used here, based on a spin echo, has been thoroughly tested against Maxwell terms (Ianuş et al., 2018) (which would mainly affect K_{aniso} estimates), as well as optimized for higher-order terms (Henriques et al., 2021b) by balancing the b-values of the different waveforms. However, the sequence is more biased to longer T_2 species due to the necessity to keep magnetization in the transverse plane during two diffusion epochs and the mixing time. Thus, it may be further biased via intra/extracellular space filtering, assuming they have different T_2s. It may be more difficult to resolve the long TE bias, as applying DDE in fully stimulated echo modes (Shemesh and Cohen, 2011) can result in significant losses in signal to noise (Kerkelä et al., 2021). Spectroscopic CTI relying on DDE spectroscopy (Shemesh et al., 2014) to elucidate the nature of its contrast with ground-truth biology and compartmentation into biologically relevant cellular-specific environments could be another valuable future perspective (Palombo et al., 2016; Shemesh et al., 2017). All these efforts are underway in the lab and will be reported in due course.

5. Conclusions

In conclusion, CTI provides enhanced specificity towards kurtosis sources, thereby potentially enhancing microstructural information on beading and edema effects in ischemia that cannot be resolved using conventional dMRI. We expect that this first study could be used as a steppingstone for developing CTI in stroke imaging and for assessing novel therapies. More generally, we expect that the CTI metrics will transcend the particular neural injury model used here, namely experimental photothrombotic ischemia, and that CTI can be generalized towards other important biological mechanisms underlying different neurological and other diseases, aging, or changes in microstructure associated with plasticity, development, learning and maturation. All these features bode well for the application of CTI in basic and applied research in the future.

Credit authorship contribution statement

Rita Alves: Data curation, Formal analysis, Investigation, Methodology, Writing – original draft, Writing – review & editing, Validation. **Rafael Neto Henriques:** Conceptualization, Formal analysis, Investigation, Methodology, Resources, Software, Writing – original draft, Writing – review & editing, Validation. **Leevi Kerkelä:** Resources, Methodology, Software, Writing – review & editing. **Cristina Chavarrías:** Visualization, Writing – review & editing, Project administration. **Sune N Jespersen:** Conceptualization, Project administration, Resources, Methodology, Supervision, Funding acquisition, Writing – original draft, Writing – review & editing, Validation. **Noam Shemesh:** Conceptualization, Project administration, Resources, Methodology, Supervision, Funding acquisition, Writing – original draft, Writing – review & editing, Validation.

Acknowledgments

Data availability

The data sets generated and analysed during the current study are freely available at https://data.mendeley.com/datasets/39gpcy7cgs/draft?a=5fe6d0be-e46c-4d07-a968-c3ea2310725c.

Code availability

Custom MATLAB code for dMRI pre- and post-processing of data is freely available at https://data.mendeley.com/datasets/39gpcy7cgs/draft?a=5fe6d0be-e46c-4d07-a968-c3ea2310725c.

Supplementary materials

Supplementary material associated with this article can be found, in the online version, at doi:10.1016/j.neuroimage.2021.118833.

References

Adluru, G., Gur, Y., Anderson, J.S., Richards, L.G., Adluru, G., DiBella, E.V.R., 2014. Assessment of white matter microstructure in stroke patients using NODDI. Conf. Proc. IEEE Eng. Med. Biol. Soc. 2014, 742–745. doi:10.1109/EMBC.2014.6943697.

Åslund, I., Nowacka, A., Nilsson, M., Topgaard, D., 2009. Filter-exchange PGSE NMR determination of cell membrane permeability. J. Magn. Reson. 200, 291–295. doi:10.1016/j.jmr.2009.07.015.

Assaf, Y., Cohen, Y., 1998. Non-mono-exponential attenuation of water and N-acetyl aspartate signals due to diffusion in brain tissue. J. Magn. Reson. 131, 69–85. doi:10.1006/jmre.1997.1313.

Astrup, J., Siesjö, B.K., Symon, L., 1981. Thresholds in cerebral ischemia - the ischemic penumbra. Stroke 12, 723–725. doi:10.1161/01.STR.12.6.723.

Baltan, S., 2014. Excitotoxicity and mitochondrial dysfunction underlie age-dependent ischemic white matter injury. Adv. Neurobiol. 11, 151–170. doi:10.1007/978-3-319-08894-5_8.

Barthel, K.U., 2012. Volume Viewer [WWW Document]. URL https://imagej.net/plugins/volume-viewer.html

Basser, P.J., Mattiello, J., LeBihan, D., 1994. MR diffusion tensor spectroscopy and imaging. Biophys. J. 66, 259–267. doi:10.1016/S0006-3495(94)80775-1.

Belov Kirdajova, D., Kriska, J., Tureckova, J., Anderova, M., 2020. Ischemia-Triggered Glutamate Excitotoxicity From the Perspective of Glial Cells. Front. Cell. Neurosci. 14. doi:10.3389/fncel.2020.00051.

Brodt, S., Gais, S., Beck, J., Erb, M., Scheffler, K., Schönauer, M., 2018. Fast track to the neocortex: a memory engram in the posterior parietal cortex. Science 362, 1045–1048. doi:10.1126/science.aau2528.

Budde, M.D., Frank, J.A., 2010. Neurite beading is sufficient to decrease the apparent diffusion coefficient after ischemic stroke. Proc. Natl. Acad. Sci. U. S. A. 107, 14472–14477. doi:10.1073/pnas.1004841107.

Budde, M.D., Janes, L., Gold, E., Turtzo, L.C., Frank, J.A., 2011. The contribution of gliosis to diffusion tensor anisotropy and tractography following traumatic brain injury: validation in the rat using Fourier analysis of stained tissue sections. Brain 134, 2248–2260. doi:10.1093/brain/awr161.

Burcaw, L.M., Fieremans, E., Novikov, D.S., 2015. Mesoscopic structure of neuronal tracts from time-dependent diffusion. Neuroimage 114, 18–37. doi:10.1016/j.neuroimage.2015.03.061.

Buscemi, L., Price, M., Bezzi, P., Hirt, L., 2019. Spatio-temporal overview of neuroinflammation in an experimental mouse stroke model. Sci. Rep. 9, 507. doi:10.1038/s41598-018-36598-4.

Callaghan, P.T., Coy, A., MacGowan, D., Packer, K.J., Zelaya, F.O., 1991. Diffraction-like effects in NMR diffusion studies of fluids in porous solids. Nature 351, 467–469. doi:10.1038/351467a0.

Callaghan, R., Alexander, D.C., Palombo, M., Zhang, H., 2020. ConFiG : contextual fibre growth to generate realistic axonal packing for diffusion MRI simulation. Neuroimage 220, 117107. doi:10.1016/j.neuroimage.2020.117107.

Campbell, B.C.V., Christensen, S., Levi, C.R., Desmond, P.M., Donnan, G.A., Davis, S.M., Parsons, M.W., 2012. Comparison of Computed Tomography Perfusion and Magnetic Resonance Imaging Perfusion-Diffusion Mismatch in Ischemic Stroke 43 (10), 2648–2653. doi:10.1161/STROKEAHA.112.660548.

Cheng, Y., Cory, D.G., 1999. Multiple scattering by NMR. J. Am. Chem. Soc. 7935–7936.

Craddock, R.C., Jbabdi, S., Yan, C.G., Vogelstein, J.T., Castellanos, F.X., Di Martino, A., Kelly, C., Heberlein, K., Colcombe, S., Milham, M.P., 2013. Imaging human connectomes at the macroscale. Nat. Methods 10, 524–539. doi:10.1038/nmeth.2482.

De Strooper, B., Karran, E., 2016. The cellular phase of Alzheimer's disease. Cell 164, 603–615. doi:10.1016/j.cell.2015.12.056.

Dietrich, W.D., Busto, R., Watson, B.D., Scheinberg, P., Ginsberg, M.D., 1987. Photochemically induced cerebral infarction. Acta Neuropathol. 72, 326–334. doi:10.1007/BF00687263.

Drobnjak, I., Siow, B., Alexander, D.C., 2010. Optimizing gradient waveforms for microstructure sensitivity in diffusion-weighted MR. J. Magn. Reson. 206, 41–51. doi:10.1016/j.jmr.2010.05.017.

Drobnjak, I., Zhang, H., Hall, M.G., Alexander, D.C., 2011. The matrix formalism for generalised gradients with time-varying orientation in diffusion NMR. J. Magn. Reson. 210, 151–157. doi:10.1016/j.jmr.2011.02.022.

Duong, T.Q., Ackerman, J.J.H., Ying, H.S., Neil, J.J., 1998. Evaluation of extra- and intracellular apparent diffusion in normal and globally ischemic rat brain via 19F NMR. Magn. Reson. Med. 40, 1–13. doi:10.1002/mrm.1910400102.

Enright, L.E., Zhang, S., Murphy, T.H., 2007. Fine mapping of the spatial relationship between acute ischemia and dendritic structure indicates selective vulnerability of layer V neuron dendritic tufts within single neurons *in vivo*. J. Cereb. Blood Flow Metab. Off. J. Int. Soc. Cereb. Blood Flow Metab. 27, 1185–1200. doi:10.1038/sj.jcbfm.9600428.

Eriksson, S., Lasic, S., Topgaard, D., 2013. Isotropic diffusion weighting in PGSE NMR by magic-angle spinning of the q -vector. J. Magn. Reson. 226, 13–18. doi:10.1016/j.jmr.2012.10.015.

Ferrer, I., Planas, A.M., 2003. Signaling of cell death and cell survival following focal cerebral ischemia: life and death struggle in the penumbra. J. Neuropathol. Exp. Neurol. 62, 329–339. doi:10.1093/jnen/62.4.329.

Fieremans, E., Jensen, J.H., Helpern, J.A., 2011. White matter characterization with diffusional kurtosis imaging. Neuroimage 58, 177–188. doi:10.1016/j.neuroimage.2011.06.006.White.

Finsterbusch, J., 2011. Chapter 6 - Multiple-Wave-Vector Diffusion-Weighted NMR, 1st ed. Elsevier Ltd Annual Reports on NMR Spectroscopy doi:10.1016/B978-0-12-385857-3.00006-2.

Franklin, K., Paxinos, G., 2019. Paxinos and franklin's the mouse brain in stereotaxic coordinates, 5th ed.

Garyfallidis, E., Brett, M., Amirbekian, B., Rokem, A., van der Walt, S., Descoteaux, M., Nimmo-Smith, I., 2014. Dipy, a library for the analysis of diffusion MRI data. Front. Neuroinform. 8. doi:10.3389/fninf.2014.00008.

Goodman, J.A., Ackerman, J.J.H., Neil, J.J., 2008. Cs + ADC in rat brain decreases markedly at death. Magn. Reson. Med. 59, 65–72. doi:10.1002/mrm.21418.

Grinberg, F., Ciobanu, L., Farrher, E., Shah, N.J., 2012. Diffusion kurtosis imaging and log-normal distribution function imaging enhance the visualisation of lesions in animal stroke models. NMR Biomed. 25, 1295–1304. doi:10.1002/nbm.2802.

Guizar-sicairos, M., Thurman, S.T., Fienup, J.R., 2008. Efficient subpixel image registration algorithms. Opt. Lett. 33, 156–158. doi:10.1364/OL.33.000156.

Henriques, R.N., 2018. Advanced Methods for Diffusion MRI Data Analysis and Their Application to the Healthy Ageing Brain. Cambridge University doi:10.17863/CAM.29356.

Henriques, R.N., Correia, M., Maralle, M., Huber, E., Kruper, J., Koudoro, S., Yeatman, J., Garyfallidis, E., Rokem, A., 2021a. Diffusional kurtosis imaging in the diffusion imaging in python project. Front. Hum. Neurosci. 19, 675433–675455. doi:10.3389/fn-hum.2021.675433.

Henriques, R.N., Jespersen, S.N., Shemesh, N., 2021b. Evidence for microscopic kurtosis in neural tissue revealed by correlation tensor MRI. Magn. Reson. Med. 86, 3111–3130. doi:10.1002/mrm.28938.

Henriques, R.N., Jespersen, S.N., Shemesh, N., 2020. Correlation tensor magnetic resonance imaging. Neuroimage 211, 116605–116622. doi:10.1016/j.neuroimage.2020.116605.

Hill, R.A., Li, A.M., Grutzendler, J., 2018. Lifelong cortical myelin plasticity and age-related degeneration in the live mammalian brain. Nat. Neurosci. 21, 683–695. doi:10.1038/s41593-018-0120-6.

Hori, N., Carpenter, D.O., 1994. Functional and morphological changes induced by transient *in vivo* ischemia. Exp. Neurol. 129, 279–289. doi:10.1006/exnr.1994.1170.

Hossmann, K.A., 2006. Pathophysiology and therapy of experimental stroke. Cell. Mol. Neurobiol. 26, 1057–1083. doi:10.1007/s10571-006-9008-1.

Hughes, E.G., Orthmann-Murphy, J.L., Langseth, A.J., Bergles, D.E., 2018. Myelin remodeling through experience-dependent oligodendrogenesis in the adult somatosensory cortex. Nat. Neurosci. 21, 696–706. doi:10.1038/s41593-018-0121-5.

Hui, E.S., Du, F., Duong, T.Q., 2012a. Spatiotemporal dynamics of diffusional kurtosis, mean diffusivity and perfusion changes in experimental stroke. Brain Res. 23, 1–7. doi:10.1038/jid.2014.371.

Hui, E.S., Fieremans, E., Jensen, J.H., Tabesh, A., Feng, W., Bonilha, L., Spampinato, M.V., Adams, R., Helpern, J.A., 2012b. Stroke assessment with diffusional kurtosis imaging. Stroke 43, 2968–2973. doi:10.1161/STROKEAHA.112.657742.

Ianuš, A., Alexander, D.C., Drobnjak, I., 2016. Microstructure imaging sequence simulation toolbox. 34–44. 10.1007/978-3-319-46630-9_4

Ianuş, A., Jespersen, S.N., Serradas Duarte, T., Alexander, D.C., Drobnjak, I., Shemesh, N., 2018. Accurate estimation of microscopic diffusion anisotropy and its time dependence in the mouse brain. Neuroimage 183, 934–949. doi:10.1016/j.neuroimage.2018.08.034.

Ianuş, A., Siow, B., Drobnjak, I., Zhang, H., Alexander, D.C., 2013. Gaussian phase distribution approximations for oscillating gradient spin echo diffusion MRI. J. Magn. Reson. 227, 25–34. doi:10.1016/j.jmr.2012.11.021.

Jelescu, I.O., Ciobanu, L., Geffroy, F., Marquet, P., Le Bihan, D., 2014. Effects of hypotonic stress and ouabain on the apparent diffusion coefficient of water at cellular and tissue levels in Aplysia. NMR Biomed. 27, 280–290. doi:10.1002/nbm.3061.

Jensen, J.H., Helpern, J.A., Ramani, A., Lu, H., Kaczynski, K., 2005. Diffusional kurtosis imaging: the quantification of non-Gaussian water diffusion by means of magnetic resonance imaging. Magn. Reson. Med. 53, 1432–1440. doi:10.1002/mrm.20508.

Jespersen, S.N., 2012. Equivalence of double and single wave vector diffusion contrast at low diffusion weighting. NMR Biomed. 813–818. doi:10.1002/nbm.1808.

Jespersen, S.N., Lundell, H., Sønderby, C.K., Dyrby, T.B., 2013. Orientationally invariant metrics of apparent compartment eccentricity from double pulsed field gradient diffusion experiments. NMR Biomed. 26, 1647–1662. doi:10.1002/nbm.2999.

Jespersen, S.N., Olesen, J.L., Ianuş, A., Shemesh, N., 2019. Effects of nongaussian diffusion on "isotropic diffusion" measurements: an *ex-vivo* microimaging and simulation study. J. Magn. Reson. 300, 84–94. doi:10.1016/j.jmr.2019.01.007.

Karbasforoushan, H., Cohen-Adad, J., Dewald, J.P.A., 2019. Brainstem and spinal cord MRI identifies altered sensorimotor pathways post-stroke. Nat. Commun. 10, 3524. doi:10.1038/s41467-019-11244-3.

Kärger, J., 1985. NMR self-diffusion studies in heterogeneous systems. Adv. Colloid Interface Sci. 23, 129–148. doi:10.1016/0001-8686(85)80018-X.

Kellner, E., Dhital, B., Kiselev, V.G., Reisert, M., 2016. Gibbs-ringing artifact removal based on local subvoxel-shifts. Magn. Reson. Med. 76, 1574–1581. doi:10.1002/mrm.26054.

Kerkelä, L., Nery, F., Callaghan, R., Zhou, F., Gyori, N.G., Szczepankiewicz, F., Palombo, M., Parker, G.J.M., Zhang, H., Hall, M.G., Clark, C.A., 2021. Comparative analysis of signal models for microscopic fractional anisotropy estimation using q-space trajectory encoding. Neuroimage 242, 118445–118457. doi:10.1016/j.neuroimage.2021.118445.

Kerkelä, L., Nery, F., Hall, M., Clark, C., 2020. Disimpy: a massively parallel Monte Carlo simulator for generating diffusion-weighted MRI data in Python. J. Open Source Softw. 5, 2527. doi:10.21105/joss.02527.

Kislin, M., Sword, J., Fomitcheva, I.V., Croom, D., Pryazhnikov, E., Lihavainen, E., Toptunov, D., Rauvala, H., Ribeiro, A.S., Khiroug, L., Kirov, S.A., 2017. Reversible disruption of neuronal mitochondria by ischemic and traumatic injury revealed by quantitative two-photon imaging in the neocortex of anesthetized Mice. J. Neurosci. 37, 333–348. doi:10.1523/JNEUROSCI.1510-16.2016.

Koch, M.A., Finsterbusch, J., 2008. Compartment size estimation with double wave vector diffusion-weighted imaging. Magn. Reson. Med. 101, 90–101. doi:10.1002/mrm.21514.

Lampinen, B., Szczepankiewicz, F., Westen, D.Van, Englund, E., Nilsson, M., Sundgren, P.C., Jimmy, L., Sta, F., 2017. Optimal experimental design for filter exchange imaging : apparent exchange rate measurements in the healthy brain and in intracranial tumors. Magn. Reson. Med. 1114, 1104–1114. doi:10.1002/mrm.26195.

Lasič, S., Szczepankiewicz, F., Eriksson, S., Nilsson, M., Topgaard, D., 2014. Microanisotropy imaging: quantification of microscopic diffusion anisotropy and orientational order parameter by diffusion MRI with magic-angle spinning of the q-vector. Front. Phys. 2, 1–14. doi:10.3389/fphy.2014.00011.

Lawrenz, M., Finsterbusch, J., 2013. Double-wave-vector diffusion-weighted imaging reveals microscopic diffusion anisotropy in the living human brain 1082, 1072–1082. 10.1002/mrm.24347

Le Bihan, D., 2007. The "wet mind": water and functional neuroimaging. Phys. Med. Biol. 52, 57–90. doi:10.1088/0031-9155/52/7/R02.

Le Bras, A., 2020. A new rat model of hydrocephalus. Lab Anim. (NY). 49, 44. doi:10.1038/s41684-020-0469-5.

Lee, H.H., Papaioannou, A., Kim, S.L., Novikov, D.S., Fieremans, E., 2020. A time-dependent diffusion MRI signature of axon caliber variations and beading. Commun. Biol. 3, 1–13. doi:10.1038/s42003-020-1050-x.

Li, N., Lee, B., Liu, R.J., Banasr, M., Dwyer, J.M., Iwata, M., Li, X.Y., Aghajanian, G., Duman, R.S., 2010. mTOR-dependent synapse formation underlies the rapid antidepressant effects of NMDA antagonists. Science 329, 959–964. doi:10.1126/science.1190287.

Mathers, C., Stevens, G., Mahanani, W.R., Ho, J., Ma Fat, D., Hogan, D., 2017. WHO methods and data sources for country-level causes of death 2000-2015 [WWW Document]. URL https://www.who.int/healthinfo/global_burden_disease/GlobalCOD_method_2000_2015.pdf?ua=1.

Mitra, P.P., 1995. Multiple wave-vector extensions of the NMR pulsed-field-gradient spin-echo diffusion measurement. Phys. Rev. 51, 74–78. doi:10.1103/physrevb.51.15074.

Moseley, M.E., Cohen, Y., Mintorovitch, J., Chileuitt, L., Shimizu, H., Kucharczyk, J., Wendland, M.F., Weinstein, P.R., 1990a. Early detection of regional cerebral ischemia in cats: comparison of diffusion- and T2-weighted MRI and spectroscopy. Magn. Reson. Med. 14, 330–346. doi:10.1002/mrm.1910140218.

Moseley, M.E., Kucharczyk, J., Mintorovitch, J., Cohen, Y., Kurhanewicz, J., Derugin, N., Asgari, H., Norman, D., 1990b. Diffusion-weighted MR imaging of acute stroke: correlation with T2-weighted and magnetic susceptibility-enhanced MR imaging in cats. Am. J. Neuroradiol. 11, 423–429.

Moura, L.M., Luccas, R., De Paiva, J.P.Q., Amaro, E., Leemans, A., Leite, C.da C., Otaduy, M.C.G., Conforto, A.B., 2019. Diffusion tensor imaging biomarkers to predict motor outcomes in stroke: a narrative review. Front. Neurol. 10, 1–17. doi:10.3389/fneur.2019.00445.

Mukherjee, P., 2005. Diffusion tensor imaging and fiber tractography in acute stroke. Neuroimaging Clin. N. Am. 15, 655–665. doi:10.1016/j.nic.2005.08.010.

Murphy, T.H., Corbett, D., 2009. Plasticity during stroke recovery: from synapse to behavior. Nat. Rev. Neurosci. 10, 861–872. doi:10.1038/nrn2735.

Nilsson, M., Lätt, J., Van Westen, D., Brockstedt, S., Lasic, S., Stahlberg, F., Topgaard, D., 2013. Noninvasive mapping of water diffusional exchange in the human brain using filter-exchange imaging. Magn. Reson. Med. 1581, 1573–1581. doi:10.1002/mrm.24395.

Nilsson, M., Szczepankiewicz, F., Brabec, J., Taylor, M., Westin, C., Golby, A., Westen, D., Sundgren, P.C., 2020. Tensor-valued diffusion MRI in under 3 min: an initial survey of microscopic anisotropy and tissue heterogeneity in intracranial tumors. Magn. Reson. Med. 83, 608–620. doi:10.1002/mrm.27959.

Nørhøj Jespersen, S., Buhl, N., 2011. The displacement correlation tensor: microstructure, ensemble anisotropy and curving fibers. J. Magn. Reson. 208, 34–43. doi:10.1016/j.jmr.2010.10.003.

Novello, L., Neto Henriques, R., Ianuş, A., Feiweier, T., Shemesh, N., Jovicich, J., 2021. Human brain *in vivo* correlation tensor MRI on a clinical 3T system. bioRxiv. 10.1101/2021.11.02.466950

Novikov, D.S., Jensen, J.H., Helpern, J.A., Fieremans, E., 2014. Revealing mesoscopic structural universality with diffusion. Proc. Natl. Acad. Sci. 111, 5088–5093. doi:10.1073/pnas.1316944111.

Novikov, D.S., Kiselev, V.G., 2010. Effective medium theory of a diffusion-weighted signal. NMR Biomed. 23, 682–697. doi:10.1002/nbm.1584.

Obata, T., Kershaw, J., Tachibana, Y., Miyauch, T., Abe, Y., Shibata, S., Kawaguchi, H., Ikoma, Y., Takuwa, H., Aoki, I., Yasui, M., 2018. Comparison of diffusion-

weighted MRI and anti-Stokes Raman scattering (CARS) measurements of the inter-compartmental exchange- time of water in expression- controlled aquaporin-4 cells. Sci. Rep. 1–11. doi:10.1038/s41598-018-36264-9.

Ozarslan, E., Westen, D.Van, Mattisson, C., Bogren, M., Donnell, O., Kubicki, M., Topgaard, D., Nilsson, M., 2016. Q-space trajectory imaging for multi-dimensional diffusion MRI of the human brain. Neuroimage 345–362. doi:10.1016/j.neuroimage.2016.02.039.

Palombo, M., Ligneul, C., Najac, C., Le, J., Flament, J., Escartin, C., 2016. New paradigm to assess brain cell morphology by diffusion-weighted MR spectroscopy *in vivo*. Proc. Natl. Acad. Sci. U. S. A 113, 6671–6676. doi:10.1073/pnas.1504327113.

Paulsen, J.L., Özarslan, E., Komlosh, M.E., Basser, P.J., Song, Y.Q., 2015. Detecting compartmental non-Gaussian diffusion with symmetrized double-PFG MRI. NMR Biomed. 28, 1550–1556. doi:10.1002/nbm.3363.

Peelaerts, W., Bousset, L., Van der Perren, A., Moskalyuk, A., Pulizzi, R., Giugliano, M., Van den Haute, C., Melki, R., Baekelandt, V., 2015. α-Synuclein strains cause distinct synucleinopathies after local and systemic administration. Nature 522, 340–344. doi:10.1038/nature14547.

Pestilli, F., Yeatman, J.D., Rokem, A., Kay, K.N., Wandell, B.A., 2014. Evaluation and statistical inference for human connectomes. Nat. Methods 11, 1058–1063. doi:10.1038/nmeth.3098.

Piao, M.S., Lee, J.K., Park, C.S., Ryu, H.S., Kim, S.H., Kim, H.S., 2009. Early activation of matrix metalloproteinase-9 is associated with blood–brain barrier disruption after photothrombotic cerebral ischemia in rats. Acta Neurochir. 151, 1649–1653. doi:10.1007/s00701-009-0431-1.

Pitts, L.H., Tsuji, M., Nishimura, M.C., Bartkowski, H., 1986. Rat middle cerebral artery occlusion: evaluation of the model and development of a neurologic examination. Stroke 7, 472–476. doi:10.1161/01.str.17.3.472.

Rorden, C., Brett, M., 2000. Stereotaxic display of brain lesions. Behav. Neurol. 12, 191–200. doi:10.1155/2000/421719.

Scholz, J., Klein, M.C., Behrens, T.E.J., Johansen-Berg, H., 2009. Training induces changes in white-matter architecture. Nat. Neurosci. 12, 1370–1371. doi:10.1038/nn.2412.

Shemesh, N., Barazany, D., Sadan, O., Bar, L., Zur, Y., Barhum, Y., Sochen, N., Offen, D., Assaf, Y., Cohen, Y., 2012. Mapping apparent eccentricity and residual Ensemble anisotropy in the gray matter using angular. Magn. Reson. Med. 806, 794–806. doi:10.1002/mrm.23300.

Shemesh, N., Cohen, Y., 2011. Overcoming apparent susceptibility-induced anisotropy (aSIA) by bipolar double-pulsed-field-gradient NMR. J. Magn. Reson. 212, 362–369. doi:10.1016/j.jmr.2011.07.015.

Shemesh, N., Jespersen, S.N., Alexander, D.C., Cohen, Y., Drobnjak, I., Dyrby, T.B., Finsterbusch, J., Koch, M.A., Kuder, T., Laun, F., Lawrenz, M., Lundell, H., Mitra, P.P., 2016. Conventions and nomenclature for double diffusion encoding NMR and MRI. Magn. Reson. Med. 87, 82–87. doi:10.1002/mrm.25901.

Shemesh, N., Rosenberg, J.T., Dumez, J., Grant, S.C., Frydman, L., 2017. Distinguishing neuronal from astrocytic subcellular microstructures using *in vivo* double diffusion encoded 1 H MRS at 21 . 1 T. PLoS ONE 1–19. doi:10.1371/journal.pone.0185232.

Shemesh, N., Rosenberg, J.T., Dumez, J.N., Muniz, J.A., Grant, S.C., Frydman, L., 2014. Metabolic properties in stroked rats revealed by relaxation-enhanced magnetic resonance spectroscopy at ultrahigh fields. Nat. Commun. 5, 1–8. doi:10.1038/ncomms5958.

Silva, M.D., Omae, T., Helmer, K.G., Li, F., Fisher, M., Sotak, C.H., 2002. Separating changes in the intra- and extracellular water apparent diffusion coefficient following focal cerebral ischemia in the rat brain. Magn. Reson. Med. 48, 826–837. doi:10.1002/mrm.10296.

Simard, J.M., Kent, T.A., Chen, M., Tarasov, K.V., Gerzanich, V., 2007. Brain oedema in focal ischaemia: molecular pathophysiology and theoretical implications. Lancet Neurol. 6, 258–268. doi:10.1016/S1474-4422(07)70055-8.

Skinner, N.P., Kurpad, S.N., Schmit, B.D., Budde, M.D., 2015. Detection of acute nervous system injury with advanced diffusion-weighted MRI: a simulation and sensitivity analysis. NMR Biomed. 28, 1489–1506. doi:10.1002/nbm.3405.

Stejskal, E.O., Tanner, J.E., 1965. Spin diffusion measurements: spin echoes in the presence of a time-dependent field gradient. J. Chem. Phys. 42, 288–292. doi:10.1063/1.1695690.

Stokum, J.A., Gerzanich, V., Simard, J.M., 2016. Molecular pathophysiology of cerebral edema. J. Cereb. Blood Flow Metab. 36, 513–538. doi:10.1177/0271678X15617172.

Stoll, G., Kleinschnitz, C., Meuth, S.G., Braeuninger, S., Ip, C.W., Wessig, C., Nölte, I., Bendszus, M., 2008. Transient widespread blood–brain barrier alterations after cerebral photothrombosis as revealed by gadofluorine M-enhanced magnetic resonance imaging. J. Cereb. Blood Flow Metab. 29, 331–341. doi:10.1038/jcbfm.2008.129.

Suter, T.A.C.S., Jaworski, A., 2019. Cell migration and axon guidance at the border between central and peripheral nervous system. Science 365, 1–8. doi:10.1126/science.aaw8231.

Szczepankiewicz, F., Lasi, S., Westen, D.Van, Sundgren, P.C., Englund, E., Westin, C., Ståhlberg, F., Lätt, J., Topgaard, D., Nilsson, M., 2015. Quantification of microscopic diffusion anisotropy disentangles effects of orientation dispersion from microstructure : applications in healthy volunteers and in brain tumors. Neuroimage 104, 241–252. doi:10.1016/j.neuroimage.2014.09.057.

Szczepankiewicz, F., Westen, D.Van, Englund, E., Westin, C., Ståhlberg, F., Lätt, J., Sundgren, P.C., Nilsson, M., 2016. The link between diffusion MRI and tumor heterogeneity : mapping cell eccentricity and density by diffusional variance decomposition (DIVIDE). Neuroimage 142, 522–532. doi:10.1016/j.neuroimage.2016.07.038.

Takeuchi, H., Mizuno, T., Zhang, G., Wang, J., Kawanokuchi, J., Kuno, R., Suzumura, A., 2005. Neuritic beading induced by activated microglia is an early feature of neuronal dysfunction toward neuronal death by inhibition of mitochondrial respiration and axonal transport. J. Biol. Chem. 280, 10444–10454. doi:10.1074/jbc.M413863200.

Thelwall, P.E., Shepherd, T.M., Stanisz, G.J., Blackband, S.J., 2006. Effects of temperature and aldehyde fixation on tissue water diffusion properties, studied in an erythrocyte ghost tissue model. Magn. Reson. Med. 289, 282–289. doi:10.1002/mrm.20962.

Torres, A.M., Taurins, A.T., Regan, D.G., Chapman, B.E., Kuchel, P.W., 1999. Assignment of coherence features in NMR q -space plots to particular diffusion modes in erythrocyte suspensions. J. Magn. Reson. 143, 135–143. doi:10.1006/jmre.1998.1701.

Umesh Rudrapatna, S., Wieloch, T., Beirup, K., Ruscher, K., Mol, W., Yanev, P., Leemans, A., van der Toorn, A., Dijkhuizen, R.M., 2014. Can diffusion kurtosis imaging improve the sensitivity and specificity of detecting microstructural alterations in brain tissue chronically after experimental stroke? Comparisons with diffusion tensor imaging and histology. Neuroimage 97, 363–373. doi:10.1016/j.neuroimage.2014.04.013.

van der Zijden, J.P., van der Toorn, A., van der Marel, K., Dijkhuizen, R.M., 2008. Longitudinal *in vivo* MRI of alterations in perilesional tissue after transient ischemic stroke in rats. Exp. Neurol. 212, 207–212. doi:10.1016/j.expneurol.2008.03.027.

Walz, W., 2016. Photochemical models of focal brain ischemia. In: Rodent Models of Stroke, pp. 291–300. doi:10.1007/978-1-4939-5620-3.

Warach, S., Chien, D., Li, W., Ronthal, M., Edelman, R.R., 1992. Fast magnetic resonance diffusion-weighted imaging of acute human stroke. Neurology 42, 1717. doi:10.1212/WNL.42.9.1717, –1717.

Warach, S., Gaa, J., Siewert, B., Wielopolski, P., Edelman, R.R., 1995. Acute human stroke studied by whole brain echo planar diffusion-weighted magnetic resonance imaging. Ann. Neurol. 37, 231–241. doi:10.1002/ana.410370214.

Watson, B.D., Dietrich, W.D., Busto, R., Wachtel, M.S., Ginsberg, M.D., 1985. Induction of reproducible brain infarction by photochemically initiated thrombosis. Ann. Neurol. 17, 497–504. doi:10.1002/ana.410170513.

Wu, D., Li, Q., Northington, F.J., Zhang, J., 2018. Oscillating gradient diffusion kurtosis imaging of normal and injured mouse brains. NMR Biomed. 31, 1–9. doi:10.1002/nbm.3917.

Wu, D., Martin, L.J., Northington, F.J., Zhang, J., 2019. Oscillating-gradient diffusion magnetic resonance imaging detects acute subcellular structural changes in the mouse forebrain after neonatal hypoxia-ischemia. J. Cereb. Blood Flow Metab. 39, 1336–1348. doi:10.1177/0271678X18759859.

Wu, D., Martin, L.J., Northington, F.J., Zhang, J., 2014. Oscillating gradient diffusion MRI reveals unique microstructural information in normal and hypoxia-ischemia injured mouse brains. Magn. Reson. Med. 72, 1366–1374. doi:10.1002/mrm.25441.

Xing, C., Arai, K., Lo, E.H., Hommel, M., 2012. Pathophysiologic cascades in ischemic stroke. Int. J. Stroke 7, 378–385. doi:10.1111/j.1747-4949.2012.00839.x.

Yang, G., Tian, Q., Leuze, C., Wintermark, M., Mcnab, J.A., 2017. Double diffusion encoding MRI for the clinic. Magn. Reson. Med. 507–520. doi:10.1002/mrm.27043.

Yang, Y., Rosenberg, G.A., 2011. Blood–brain barrier breakdown in acute and chronic cerebrovascular disease. Stroke 42, 3323–3328. doi:10.1161/STROKEAHA.110.608257.

Zatorre, R.J., Fields, R.D., Johansen-Berg, H., 2012. Plasticity in gray and white: neuroimaging changes in brain structure during learning. Nat. Neurosci. 15, 528–536. doi:10.1038/nn.3045.

Zeiler, S.R., Hubbard, R., Gibson, E.M., Zheng, T., Ng, K., O'Brien, R., Krakauer, J.W., 2016. Paradoxical motor recovery from a first stroke after induction of a SEcond stroke. Neurorehabil. Neural Repair 30, 794–800. doi:10.1177/1545968315624783.

Zhang, H., Schneider, T., Wheeler-Kingshott, C.A., Alexander, D.C., 2012. NODDI: practical *in vivo* neurite orientation dispersion and density imaging of the human brain. Neuroimage 61, 1000–1016. doi:10.1016/j.neuroimage.2012.03.072.